U5570

NATIONAL AERONAUTICS AND SPACE ADMINISTRATION

Space Programs Summary 37-56, Vol. I

Flight Projects

For the Period January 1 to February 28, 1969

JET PROPULSION LABORATORY
CALIFORNIA INSTITUTE OF TECHNOLOGY
PASADENA, CALIFORNIA

March 31, 1969

31

NATIONAL AERONAUTICS AND SPACE ADMINISTRATION

Space Programs Summary 37-56, Vol. I

Flight Projects

For the Period January 1 to February 28, 1969

JET PROPULSION LABORATORY
CALIFORNIA INSTITUTE OF TECHNOLOGY
PASADENA, CALIFORNIA

March 31, 1969

SPACE PROGRAMS SUMMARY 37-56, VOL. I

Prepared Under Contract No. NAS 7-100
National Aeronautics and Space Administration

Preface

The Space Programs Summary is a multivolume, bimonthly publication that presents a review of technical information resulting from current engineering and scientific work performed, or managed, by the Jet Propulsion Laboratory for the National Aeronautics and Space Administration. The Space Programs Summary is currently composed of four volumes:

Vol. I. *Flight Projects* (Unclassified)

Vol. II. *The Deep Space Network* (Unclassified)

Vol. III. *Supporting Research and Advanced Development* (Unclassified)

Vol. IV. *Flight Projects and Supporting Research and Advanced Development* (Confidential)

Contents

PLANETARY–INTERPLANETARY PROGRAM

I. *Mariner* Mars 1969 Project

PLANETARY–INTERPLANETARY PROGRAM

A. Introduction

1. Mission Description

The primary objective of the *Mariner* Mars 1969 Project is to make two flyby exploratory investigations of Mars in 1969, which will set the basis for future experiments—particularly those relevant to the search for extraterrestrial life. The secondary objective is to develop Mars mission technology.

The spacecraft design concept is modeled after the successful *Mariner IV* spacecraft, considerably modified to meet the 1969 mission requirements and to enhance mission reliability.

The launch vehicle is the *Atlas/Centaur* SLV-3C, used for the *Surveyor* missions. This vehicle, developed by General Dynamics/Convair Company for the Lewis Research Center, has single- or double-burn capability in its second stage and a considerably increased performance rating over the *Atlas D/Agena D* used in the *Mariner IV* mission.

Mariner Mars 1969 missions are supported by the Air Force Eastern Test Range (AFETR), the Deep Space Network (DSN), and other NASA facilities.

The six planetary-science experiments selected by NASA for the *Mariner* Mars 1969 missions are listed in Table 1.

2. Project Status

Mariner VI was launched at 01:29:02.013 GMT, February 25, 1969, 15 min after the opening of the first launch window. The space vehicle, consisting of the *Atlas/Centaur* AC-20 and M69-3 spacecraft, performed normally with the exception of a faulty accelerometer which actuated *Atlas* booster engine cutoff early, thus causing a potential deficit in injection energy (made up later in the powered flight). Event times are given in Table 2.

Sun acquisition occurred at 01:58 GMT, about 2 min after the spacecraft left the earth's shadow. Canopus acquisition search began at 0525 GMT and was completed at 05:42; 3 min later, the gyros were turned off and the spacecraft was in cruise mode.

Launch-phase tracking and telemetry acquisition were supported by (1) the AFETR downrange network of land-based stations and the Range Instrumentation Ship Twin Falls, (2) the Manned Space Flight Network (MSFN) stations at Bermuda and Ascension Islands,

Table 1. *Mariner* Mars 1969 science experiments and investigations

Experiment	Investigator	Affiliation
Television	R. B. Leighton[a]	CIT
	B. C. Murray	CIT
	R. P. Sharp	CIT
	N. H. Horowitz	CIT
	A. G. Herriman	JPL
	R. K. Sloan	JPL
	M. E. Davies	Rand Corp.
	C. Leovy	University of Washington
	B. A. Smith	New Mexico State University
Infrared spectrometer	G. C. Pimentel[a]	UCB
	K. C. Herr	UCB
Ultraviolet airglow spectrometer	C. A. Barth[a]	University of Colorado
	F. C. Wilshusen	University of Colorado
	K. Gause	University of Colorado
	K. K. Kelly	University of Colorado
	R. Ruehle	University of Colorado
	J. B. Pearce	University of Colorado
	E. F. Mackey	Packard-Bell Electronics Corp.
	W. G. Fastie	Johns Hopkins University
Infrared radiometer	G. Neugebauer[a]	CIT
	G. Munch	CIT
	S. C. Chase	Santa Barbara Research Center, Hughes Aircraft Co.
S-band occultation	A. J. Kliore[a]	JPL
	G. Fjeldbo	Stanford University/JPL
	S. I. Rasool	Goddard Institute of Space Studies
Celestial mechanics	J. D. Anderson[a]	JPL
	W. L. Martin	JPL

[a]Principal investigator

Table 2. *Mariner VI* launch summary

Launch-phase event	GMT
Atlas booster cutoff	01:31:29.2
Atlas staging	01:31:32.2
Centaur insulation panel jettison	01:32:13.8
Nose-fairing jettison	01:32:50.6
Atlas sustainer cutoff	01:33:33.0
Atlas/Centaur separation	01:33:34.9
Centaur start	01:33:44.4
Centaur cutoff	01:41:07.6
Spacecraft separation	01:42:42.7
Start *Centaur* reorientation	01:47:14.1
Start *Centaur* blowdown	01:55:17.7

which filled the mid-Atlantic gap in DSN coverage caused by the extreme southerly latitude of the spacecraft, and (3) the short range DSS 51, which acquired the *Mariner VI* signal at 01:55 GMT.

During the next three days, telemetry indicated the spacecraft's condition to be excellent, while ranging and doppler tracking revealed the trajectory to be on the 1σ dispersion ellipse for the injection aiming point. A very small, relatively, thrust maneuver was indicated in order to bring the flight path to the desired post-maneuver aiming point (which differs from the injection aim point to assure planetary quarantine).

The maneuver was executed at 23:19 GMT on February 28. The spacecraft pitched negatively 23.45 deg, rolled 78.72 deg, and fired the on-board propulsion subsystem for 5.35 s, which changed its velocity by 3 m/s. The spacecraft then reacquired the sun and Canopus. It had not pitched far enough off the sun line to interrupt the solar power mode.

During and following the motor burn, the Canopus sensor, which remained on (but not in the control loop) throughout the maneuver for the first time in a *Mariner* mission, detected brightness sources thought to be either dispersed rocket-exhaust gases, or, more likely, dust particles dislodged from the spacecraft. During the commanded squib-firing event, which unlatched the scan platform on March 6, a similar event occurred causing the attitude control system to lose Canopus acquisition. A normal roll-search reacquisition was accomplished immediately without recourse to any ground commands.

The spacecraft condition and performance throughout the early phases of the flight continued to be excellent, and mission operations and tracking and data acquisition were equally good.

B. Project Engineering

1. Spacecraft System Test and Launch Operations

a. Introduction. All scheduled *Mariner* Mars 1969 spacecraft system test and launch operations were completed during January and February 1969. However, because of problems with the *Atlas/Centaur* AC-19 launch vehicle and the M69-2 spacecraft, the first launch opportunity (launch F) was met using spacecraft M69-3 and the AC-20 launch vehicle from Launch Complex 36B.

b. Spacecraft M69-2

Spacecraft–system test complex compatibility test. On January 6, 1969 the interface compatibility of the M69-2 spacecraft and System Test Complex 2 in the Air Force Eastern Test Range (AFETR) Building AO was verified.

System Test 4. System Test 4 (AFETR System Test 1) was conducted on January 8–17. The purpose of the test was to verify the functional performance of the spacecraft as an integrated system within the constraints imposed by test equipment and the earth-based environment. During the test, the spacecraft was operated in all major modes of the nominal flight sequence. In preparation for the system test, the television/data storage interface was verified using data from a television simulator. During the system test, a fixed sequencer trajectory-correction maneuver was performed in which the motor burn time was too short when compared to the commanded value. It is suspected that either the flight command subsystem or central computer and sequencer (CC&S) subsystem were at fault. Attempts to duplicate the problem were unsuccessful.

Scan platform instrument alignment verification. In conjunction with System Test 4, a scan platform instrument alignment verification was performed on January 15–16. The line-of-sight of each planetary instrument mounted on the spacecraft scan platform was measured with respect to a reference plane on the scan platform.

Spacecraft/Cape Kennedy Compatibility Test Station compatibility verification. On January 17, the functional and operational compatibility of the interfacing elements of the spacecraft, Mission Operations System (MOS), and Deep Space Network (DSN) systems was verified.

Attitude control leak test. The M69-2 spacecraft was moved to the AFETR Explosive Safe Facility (ESF) on the morning of January 18. An attitude control leak test was performed on January 18–22 to verify the ability of the attitude control subsystem pressure vessels to maintain flight pressure and to measure nitrogen leak rates.

Decision to launch M69-3 instead of M69-2. On January 22, a decision was made to substitute M69-3 for M69-2 for the launch F (February 24) opportunity. This decision was arrived at due to the problems encountered with several M69-2 subsystems during System Test 4, notably the problem of the incorrect fixed-sequencer motor burn duration during a simulated trajectory-correction maneuver.

Equipment change-out and interface reverification. After the decision was reached to substitute M69-3 for M69-2, the period of January 23–February 6 became available for change-out of spacecraft subsystems that had demonstrated performance anomalies during System Test 4. In addition, certain equipment preferred for use for the launch F opportunity (e.g., the far-encounter planet sensor, and infrared spectrometer) were removed from M69-2 and installed on M69-3. As equipment was returned from subsystem laboratories and installed on the spacecraft, every function passing through every connector that had been demated was reverified.

System Test 5. A system test was performed on February 6–12 to demonstrate the functional performance of the new equipment within the spacecraft/system environment. During the test, the newly installed subsystems were operated in the nominal flight sequence in both the prime and redundant modes.

Final Building AO electrical and mechanical operations. Final preparation of the spacecraft for launch was performed in Building AO on February 13–17. Preparations included installation and flow testing of the attitude control flight gas nozzles, final sun sensor and gas-jet phasing verification, installation of the flight battery, solar-panel deployment tests, verification of proper scan platform motion in response to ground commands, and stowing of the scan platform in its launch position. Spacecraft weight during final preparation was 848.48 lb.

ESF electrical and mechanical operations. The M69-2 was moved to the ESF on February 18 for final launch preparation. During the period of February 18–22, the propulsion subsystem and flight pyrotechnics were installed, high-pressure gas vessels were pressurized, final electrical tests were performed (e.g., autopilot and jet-vane phasing verification), and the spacecraft was mated to its adapter and encapsulated in the *Centaur* nose fairing. Precountdown tests were conducted before and after encapsulation to verify spacecraft performance.

Standby in support of M69-3 launch operations. The M69-2 remained in the ESF on standby in support of M69-3 launch and flight during the remainder of February.

c. Spacecraft M69-3

Shipment to AFETR. The M69-3 spacecraft left JPL on January 2 in an escorted convoy of three air-ride

electronics moving vans and arrived at the AFETR on January 5.

Arrival inspection and installation in Building AO. A careful visual inspection of the spacecraft was performed following its arrival at AFETR Building AO. The spacecraft was installed on its low-level positioner in the Building AO high-bay area.

Preparation for system test. The M69-3 was assembled to the system test configuration during the period January 7–10.

Postshipment verification tests. Several verification tests were performed on January 13–15 to demonstrate the compatibility of M69-3 with System Test Complex 2 and DSS 71. In addition, the television/data storage subsystem interface was verified using television subsystem simulator data.

System test 3. During the period January 16–23, M69-3 System Test 3 (AFETR System Test 1) was conducted to verify the functional performance of the spacecraft as an integrated system. All major parts of the nominal flight sequence were tested, including several types of encounter sequences and trajectory-correction maneuvers. Because of the decision to substitute M69-3 for M69-2 during the launch F opportunity, system testing of M69-3 was accelerated through the use of two-shift operations.

Scan platform instrument alignment verification. Scan platform instrument alignments were reverified on M69-3 on January 17, 20, and 23. The line-of-sight of each planetary instrument was measured.

Attitude control leak test. The spacecraft was moved to the ESF January 24. The attitude control leak test was performed during the period January 24–27.

Final Building AO electrical and mechanical operations. Final preparation of the spacecraft for launch was performed in Building AO January 28–February 3. The M69-3 preparations were identical to those performed on M69-2. In addition to spacecraft weight, the X–Y plane center of gravity was also measured. Measured spacecraft weight was 850.31 lb; the measured spacecraft center-of-gravity location was $\bar{X}$ + 0.14 in., $\bar{Y}$ = + 0.57 in., and $\bar{Z}$ = 13.92 in.

ESF electrical and mechanical operations. The M69-3 was moved to ESF February 4. Prelaunch preparations performed at the ESF February 4–11 were identical to those performed for M69-2.

Mate with launch vehicle. On February 12, M69-3 was moved to Launch Complex 36A and mated to *Atlas/Centaur* AC-19. An on-pad verification was performed to demonstrate spacecraft compatibility with launch complex equipment and the launch complex environment.

Precountdown. A precountdown test was performed on February 13. The purpose of the precountdown was to perform the most detailed spacecraft verification permitted within the limits of the launch configuration and the launch-complex equipment. No significant problems were encountered during the precountdown test.

Countdown during launch vehicle EMI/RFI test. A launch countdown test was performed February 14 to provide additional training for personnel involved in the actual launch of M69-3 and to verify the countdown procedure that would be used. The countdown was performed in conjunction with an electromagnetic interference/radio-frequency interference (EMI/RFI) test performed with the launch vehicle. Spacecraft telemetry was carefully monitored to verify that the EMI/RFI environment had no effect on data readouts. Shortly after completion of the test, the launch vehicle (AC-19) suffered major damage due to partial loss of the pressure used to maintain structural rigidity. The spacecraft was demated from the launch vehicle, returned to the ESF, and de-encapsulated in preparation for a thorough investigation of its condition.

Spacecraft verification test. A comprehensive verification of all subsystems that may have been affected by the motion imparted to the spacecraft when the launch vehicle temporarily lost pressure was performed on February 15 and 16. No anomalies were observed.

The spacecraft was re-encapsulated on February 17 and an abbreviated precountdown was performed to verify spacecraft functional performance.

Mate with launch vehicle. The M69-3 was moved to Launch Complex 36B on February 18 and mated with the *Atlas/Centaur* AC-20 launch vehicle. An on-pad verification based upon the precountdown test was performed to demonstrate spacecraft compatibility with the launch vehicle and the launch complex environment.

Countdown during operational readiness test. On February 19, a practice countdown was performed in

conjunction with the MOS final operational readiness test. Based on data obtained during the practice countdown, the launch countdown procedure was finalized.

Precountdown. The launch precountdown was performed on February 20–21. The precountdown provided a final detailed spacecraft verification prior to launch and included careful examination of science subsystem instruments.

Countdown. The M69-3 launch countdown was performed on February 24. The spacecraft portion of the countdown went smoothly, terminating with the launch of M69-3 (*Mariner VI*) at 01:29:02.013 GMT, February 25. The launch occurred 15 min after the opening of the first launch window because of holds caused by a launch vehicle guidance system problem.

d. Spacecraft M69-4 (flight spare)

ESF electrical and mechanical operations. During the period of December 23, 1968 through January 8, 1969, the M69-4 was prepared at the ESF for launch pad testing. Operations included installation of the propulsion subsystem (filled with water instead of propellant) and flight pyrotechnics (except for adapter V-band), pressurization of high-pressure gas vessels to one-half of their flight pressures (except for the IRS gas tanks, which were at flight pressure to test on-pad monitoring instrumentation), mating of the spacecraft with its launch-vehicle adapter, encapsulation of the spacecraft in the *Centaur* nose fairing, and the performance of precountdown exercises both before and after spacecraft encapsulation. The M69-4 was used for the initial period of on-pad testing with the launch vehicles to minimize the exposure of the flight spacecraft to the relatively unknown launch pad environment, and also to provide additional time for a detailed examination of the flight spacecraft prior to their commitment to launch.

Launch complex 36A operations. Early in the morning of January 9, the M69-4 was moved from the ESF to Launch Complex 36A where it was mated to the *Atlas/Centaur* AC-19 launch vehicle. Following initial launch pad checkout, a precountdown exercise was performed on January 9 and 10 to verify spacecraft performance in the launch complex environment Countdown exercises were performed on January 14 and 15 to develop the procedures to be used for the launch of the flight spacecraft and to determine the effects of the launch complex environment, particularly EMI, on spacecraft launch operations. During the countdown test on January 15, held in conjunction with the launch vehicle flight control and propellant tanking integrated test, a problem was encountered in loading the CC&S memory from the launch complex equipment in the blockhouse. A second countdown exercise was performed on January 21 in conjunction with the launch vehicle flight acceptance composite test.

Launch complex 36B operations. On January 22, the spacecraft was removed from the AC-19 launch vehicle on Launch Complex 36A and installed on the AC-20 launch vehicle on Launch Complex 36B. Launch Complex 36B operations included a spacecraft/launch complex compatibility test on January 22, a precountdown test on January 23, and a spacecraft countdown in conjunction with a launch vehicle flight acceptance composite test on January 24. The CC&S memory loading problem was again experienced and resolved by a minor modification to the CC&S blockhouse equipment. During the spacecraft countdown exercise, the spacecraft was irradiated by the AFETR EMI sources that would be operating during the actual launch. No anomalous spacecraft performance was observed.

Attitude control leak test. The spacecraft was returned to the ESF on January 24 following the completion of Launch Complex 36B operations. An attitude control leak test was performed on January 25–29 to verify the flight readiness of the M69-4 gas systems and to measure their leakage rates.

Disassembly and inspection. The spacecraft was moved to Building AO on January 29. During the period of January 30–February 14, the spacecraft was completely disassembled, inspected for physical damage, and cleaned.

Reassembly. On February 17–19, M69-4 was reassembled to the system test configuration. A brief electrical checkout on February 20 verified the operational readiness of the spacecraft. The spacecraft remained in the system test configuration from February 21 to 26 in support of the M69-3 launch and flight operations.

System Test 3. System Test 3 (AFETR System Test 1) was started on February 28, and was scheduled for completion in early March.

C. Systems

1. Systems Analysis

a. Trajectory analysis. A contingency targeting plan has been developed to allow for emergency extension of

the basic launch date/arrival date (LD/AD) targeting plan discussed in SPS 37-52, Vol. I, pp. 8–9. This plan consists of the 20 LD/AD combinations listed in Table 3. It should be noted that the contingency arrival dates beyond August 5, 1969 result in less desirable missions than those associated with the prime arrival dates discussed in SPS 37-52, Vol. I.

Table 3. Contingency-targeting-plan LD/AD combinations

LD/AD	LD/AD
Apr 8/Aug 5	Apr 20/Oct 12
Apr 9/Aug 5	Apr 21/Oct 12
Apr 10/Sept 6	Apr 29/Nov 29
Apr 11/Sept 6	May 1/Nov 29
Apr 12/Sept 6	May 3/Nov 29
Apr 13/Sept 6	May 5/Nov 29
Apr 14/Sept 6	May 10/Jan 3
Apr 15/Sept 6	May 12/Jan 3
Apr 17/Oct 4	May 14/Jan 3
Apr 18/Oct 4	May 16/Jan 3

Four additional launch dates have been targeted for July 31, 1969 arrival date. These additional launch dates were targeted in order to maintain adequate launch probabilities in the event of launch support conflicts with *Apollo 9*.

It was decided to eliminate the February 23 LD/July 29 AD case from the launch period and to reduce the February 24, 25, and 26 launch window durations from 1 h to 40 min. The February 23 launch date was eliminated in order to base the earliest launch opportunity on the preferred arrival date of July 31. The first three launch windows for the July 31 arrival date were reduced in order to more optimally time central computer and sequencer (CC&S) events near encounter, to improve near-earth tracking geometry, and to simplify the launch countdown operations of the spacecraft. The 20-min launch window reductions on these three days resulted in a small loss in launch probability, which was considered an acceptable penalty in order to obtain the improvements mentioned above.

The trajectory design considerations and key trajectory parameters for the preferred LD/AD combinations have been formulated.[1] Figures 1 and 2 present the heliocentric trajectories for the *Mariner F* (*Mariner VI*) and *Mariner G* missions.

The last official *Mariner* Mars 1969 Performance and Trajectory Panel meeting was held at the Lewis Research Center on January 23.

b. Flight-path analysis. Orbit determination accuracy studies for the pre-maneuver, post-maneuver, encounter, and post-encounter phases of the mission have defined the effects of uncertainties in physical constants and tracking station locations, as well as data bias effects on target parameters.[2] Due to the instability of the *Mariner* Venus 67 encounter orbit solutions, a major study was undertaken to seek an operational strategy for the *Mariner* Mars 1969 orbit determination processes for encounter. Three possible strategies were formulated. Further analyses will be made before the final selection.

The final pre-launch mission maneuver strategy has been documented.[3] Figure 3 illustrates one of the operational tools used to help select the aiming point. The boundaries of aiming zones I and II are approximate. Relative science value contours are also shown in Fig. 3.

The Flight Path Analysis and Command (FPAC) group participated in six mission operations simulations of the launch and midcourse phases of the mission. These tests, and the extensive FPAC-supported software checkout, demonstrated FPAC's readiness to support the launch. The actual launch and maneuver of *Mariner VI* was supported by FPAC in accordance with the operational profile illustrated in Figure 4. Post-maneuver orbit determination of *Mariner VI* is still in process; however, present indications are that the flight path is near-nominal.

c. Encounter planning and analysis. Encounter planning proceeded during meetings of four groups: the Encounter Sequence Planning Group (ESPG), the *Mariner* Orbit Determination Encounter Study Team (MODEST), the principal investigators, and the cartographic working group.

The ESPG activity was devoted to further refinement of the encounter design (described in SPS 37-54, Vol. I,

[1] *Mariner Mars 1969 Post-Injection Standard Trajectory Document*, January 1969 (JPL internal document).

[2] *Mariner Mars 1969 Orbit Determination Strategy and Accuracy Document*, February 15, 1969 (JPL internal document).

[3] *Mariner Mars 1969 Midcourse Maneuver Strategy and Accuracy Document*, February 15, 1969 (JPL internal document).

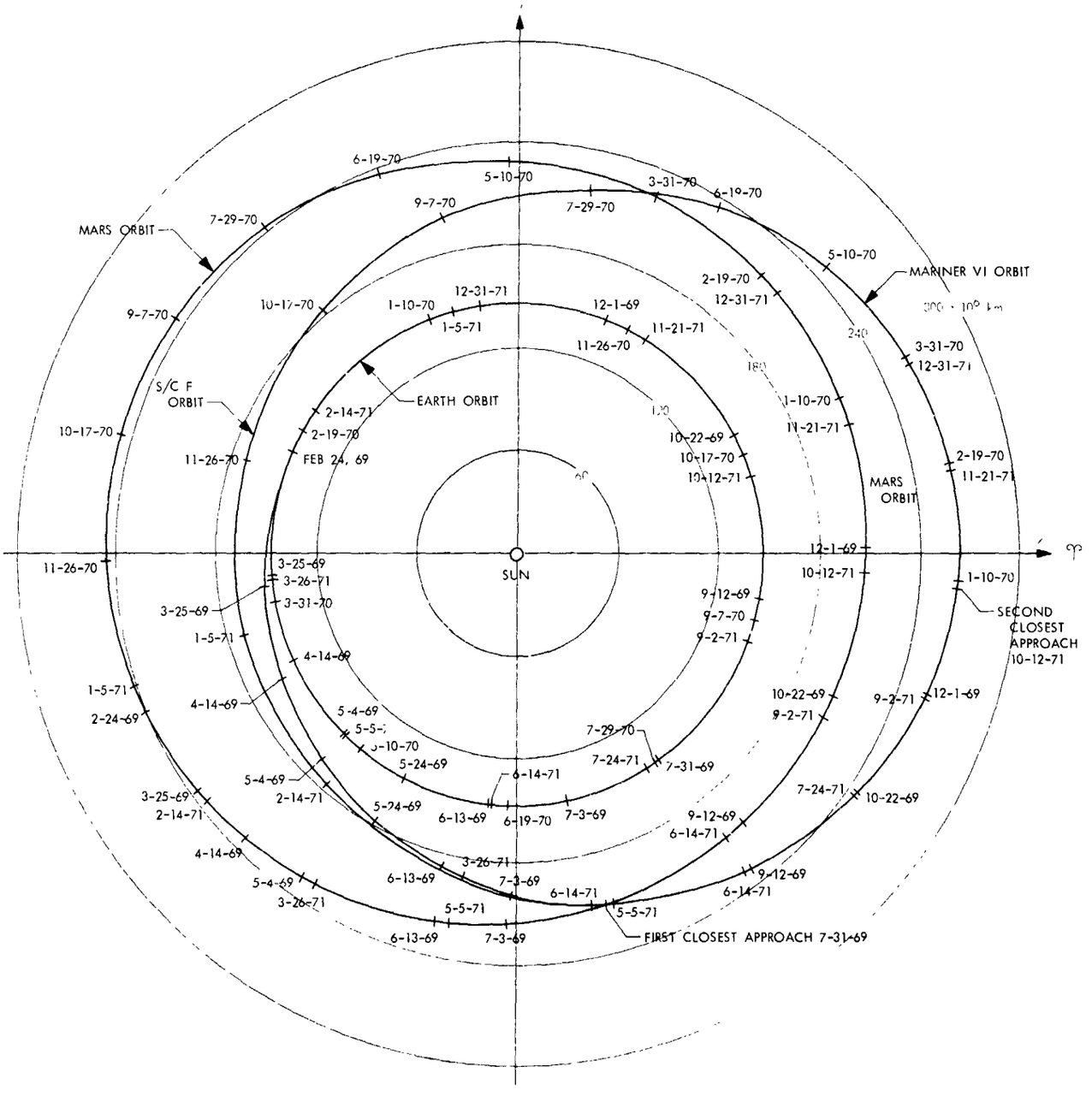

Fig. 1. Heliocentric trajectory of *Mariner VI*

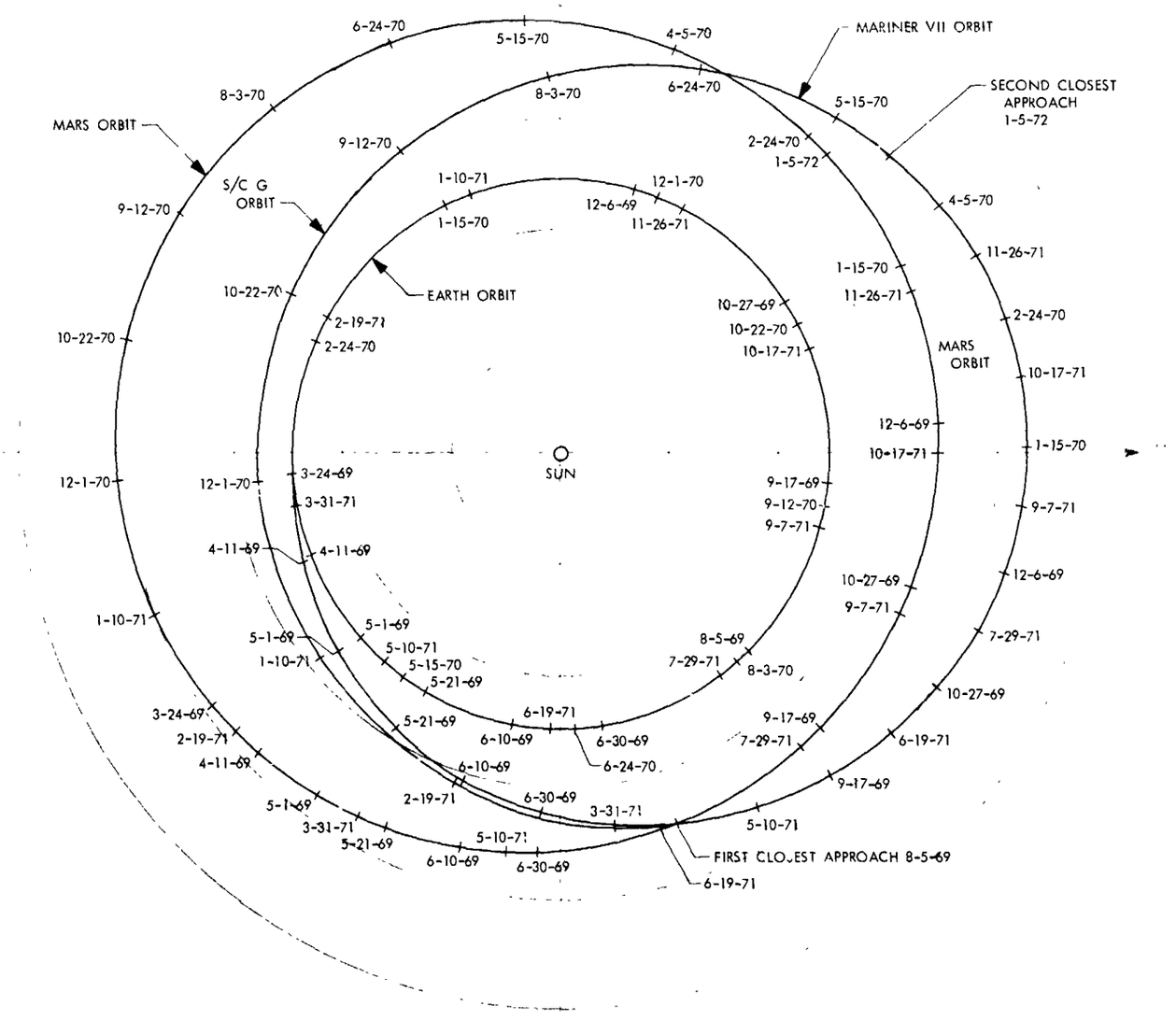

Fig. 2. Heliocentric trajectory of *Mariner VII*

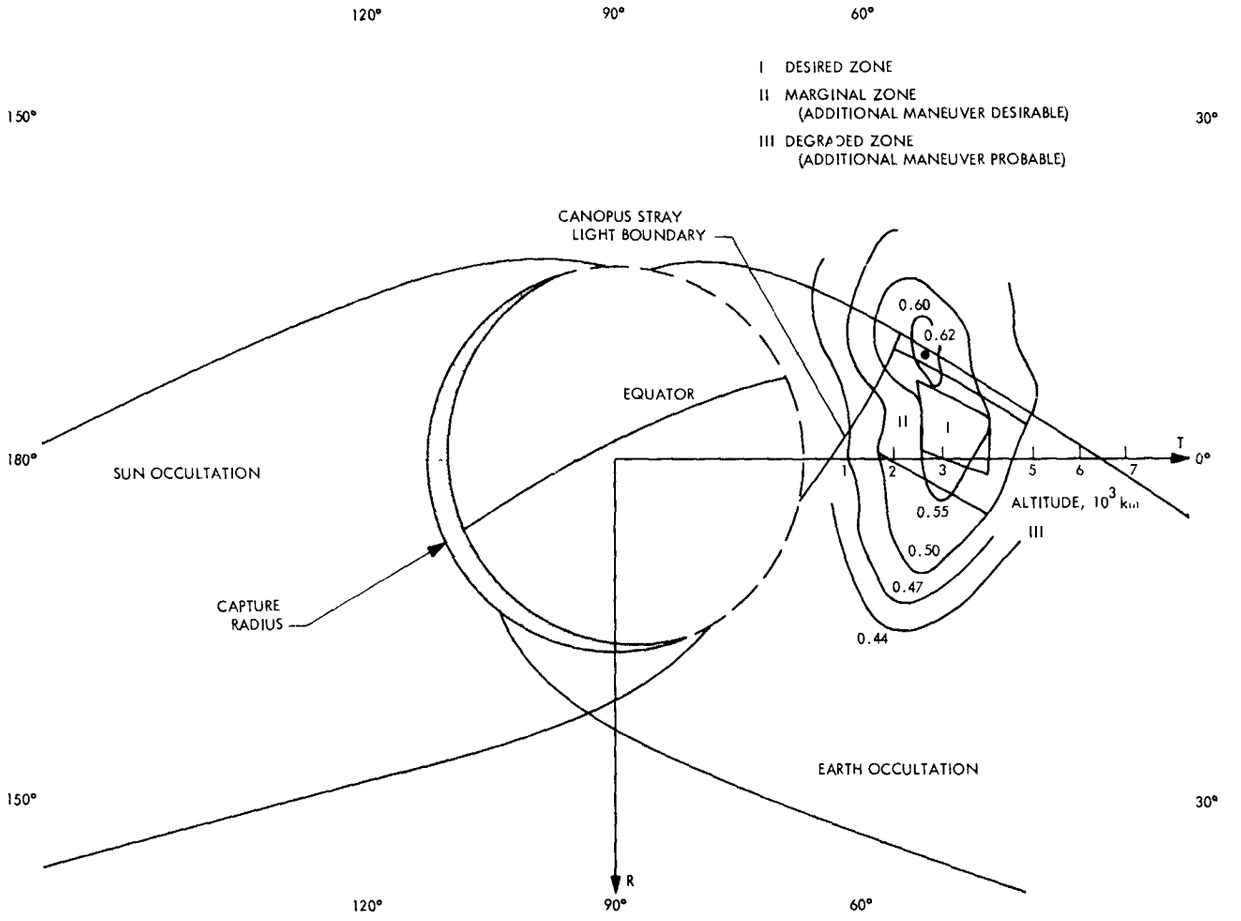

Fig. 3. Preferred aiming zones and overall science value contours (February 24 LD/July 31 AD)

pp. 5–12), with emphasis on the operational aspects and following a new set of guidelines defining the standard mission.

The MODEST was organized to perform the following tasks:

(1) To develop the strategies to be used by the single- and double-precision orbit determination programs during the encounter phase.

(2) To develop criteria for changing software, as required, to allow maximum accuracy in pre-encounter orbits.

(3) To recommend optimum tracking schedules for Deep Space Network utilization.

Intensive activity will begin after both spacecraft maneuvers. Meaningful simulations should result in final encounter strategy definition by July 1.

Timing and polar motion predictions can cause orbit determination errors. Timing polynomial coefficients must be incorporated in the single-precision orbit determination program and updated periodically. A program to correct for ionization effects is being generated. Currently, it seems very desirable to incorporate this program into the SFOF software system, in April or May, to facilitate both the handling of the output and its transfer to the other FPAC programs.

Some work is currently under way to define desirable tracking patterns; the encounter phase should see continuous tracking, whereas the cruise phase must accommodate the schedules of other projects.

Several meetings have been held with the principal investigators to exchange trajectory information and to seek identification of aiming zones. Similar exchanges of information were made during mission operations tests

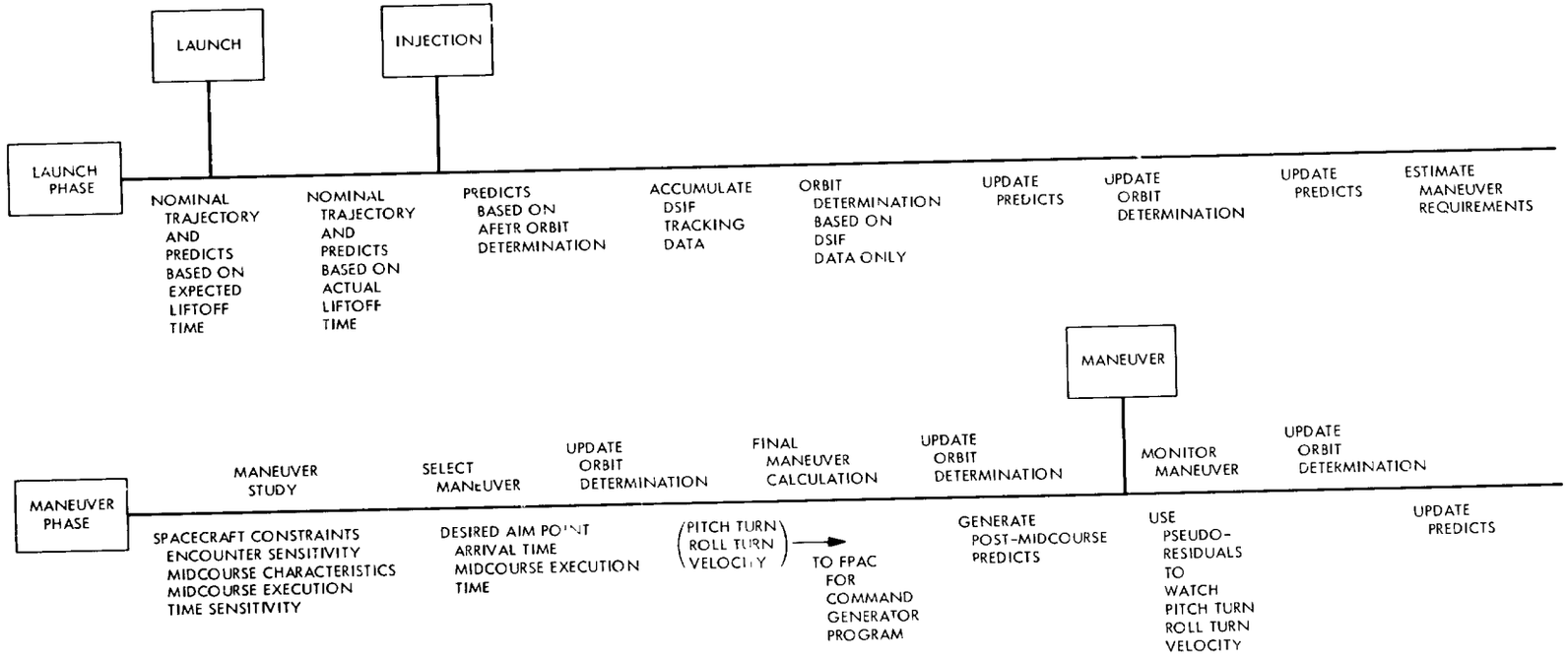

Fig. 4. FPAC launch and maneuver operational profile

of the maneuver phase and during the actual *Mariner VI* pre-maneuver conference. The latter activity led to the aiming point selection used in the definition of the *Mariner VI* maneuver.

Another part of the encounter analysis activity has been the generation of science value functions.[4] These functions were used as aids in the aiming pointing selection for *Mariner VI* (Fig. 3).

A *Mariner* Mars 1969 cartographic working group has been formed under the chairmanship of M. E. Davis of the RAND Corporation. This group explores the cartographic potential in connection with the *Mariner* Mars 1969 TV data and includes the participation of representatives from the Aeronautical Chart and Information Center, Army Map Service, US Geological Survey, as well as JPL. The proposed objectives are to utilize the TV picture data as follows:

(1) To improve the knowledge of the Mars spin-axis orientation.

(2) To establish a planet-wide coordinate control system to be utilized in the generation of detailed Mars maps.

(3) To improve the figure of the Mars surface from the determination of Mars-surface feature elevations.

d. Mission analysis. Changes in the targeting plan, refinements in trajectory information and science objectives, and minor corrections to the mission requirements reflecting hardware changes have been documented.[5]

2. UNIVAC 1219 Data Processing System

The development work described in SPS 37-55, Vol. I, pp. 4–5, to provide processing and photographic display of the TV subsystem calibration data by use of the UNIVAC 1219/TV-1 System was completed during this reporting period. Most of the period was spent in further modifications to hardware and software to overcome the problems discussed in SPS 37-55, Vol. I, and to allow step-by-step visibility into the processing through its various stages.

The processing and reformatting system is now considered operational and production has commenced. Validation of the prime calibration data recorded on FM analog magnetic tape, as well as the first processing step to produce digital log tapes, is performed by duplicate processing of the prime data. The output results on log tapes must compare closely before the subsequent processing step is taken to produce the intermediate master tape. The master tape provides records with format corrections to accommodate most of the discrepancies associated with deficient input data. The master tape is then processed further to provide calibration tapes for the Image Processing Laboratory (IPL) in a standard IPL calibration format. Pictures of the TV calibration data to accompany the tapes are now made from the final calibration data tapes themselves, rather than from the master tape as previously described.

When completed (about May 1969), this effort is expected to produce about 2000 separate digital calibration tapes and 30,000 pictures (150,000 70-mm prints) from TV-1. (By February 1, about 10,000 pictures had been produced by TV-1.) Although this effort has been difficult and time consuming, it is currently proceeding satisfactorily and an average of four to five analog tapes per day will be processed to provide about 30 IPL-formatted digital calibration tapes and the associated pictures.

The UNIVAC 1219 system Proof Test Model system test support began on January 20, 1969. During this reporting period, 28 days of support operations were provided, with 205 h of on-line operation. This support will continue, as required, until termination of the project.

D. Telecommunications

1. Telemetry Simulator

a. Introduction. The telemetry simulator is part of the operational support equipment at the six deep space stations (DSSs) of the Deep Space Instrumentation Facility involved in tracking the *Mariner* Mars 1969 spacecraft. These stations are as follows:

(1) DSS 14 (Barstow, Calif.).

(2) DSS 12 (Barstow, Calif.).

(3) DSS 41 (Woomera, Australia).

(4) DSS 51 (Johannesburg, South Africa).

(5) DSS 62 (Cebreros, Spain).

(6) Cape Kennedy Compatibility Test Station (Cape Kennedy, Fla.).

[4] *Mariner Mars 1969 Science Value Functions and Aiming Point Constraints Document*, December 1968 (JPL internal document).

[5] *Mariner Mars 1969 Mission Plan and Requirements Document, Part I, Revision 1*, February 1969 (JPL internal document).

As part of the mission-dependent equipment (MDE) located in a regular high-bay rack, the telemetry simulator has two primary functions: (1) train DSS personnel in the operation of the facility equipment during the various spacecraft flight modes, and (2) provide hardware and software verification of both the DSS and the telemetry and command processor (TCP).

b. Mechanical design. The electronic circuitry of the telemetry simulator is packaged in two 19-in. wide standard relay-rack enclosure drawers (Fig. 5) designed to accommodate 47 printed circuit boards. Drawer A1 contains 40 integrated-circuit-and-discrete-component boards. Drawer A2 contains seven discrete component cards and five modular power supplies, which provide approximately 4 A at 115 V ac. Each modular power supply has built-in over-current protection. In addition, a circuit breaker is inserted in the ac power input line and another in the logic supply output. An overvoltage load-protector is combined with the logic supply circuit breaker to provide voltage and current protection for the integrated-circuit networks. The estimated total weight is 120 lb.

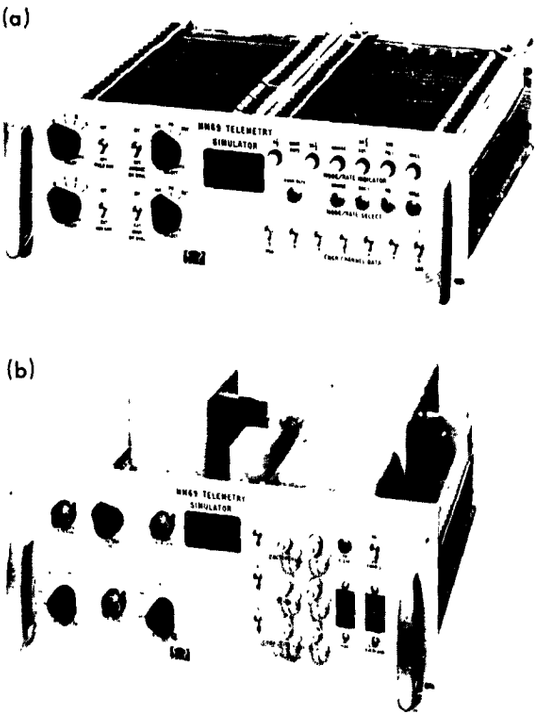

Fig. 5. *Mariner* Mars 1969 telemetry simulator

c. Functional description. The telemetry simulator is designed to duplicate the modulation algorithms of the composite telemetry signal output of the *Mariner* Mars 1969 flight telemetry subsystem (FTS). The composite signal levels can be adjusted without changing the modulation algorithms, which allows transmitters of various modulation sensitivities to be used. Figure 6 shows the voltages required to drive a transmitter with a 1-rad/V peak modulation sensitivity. The ratios 9.4:91.4 and 38.5:62.3 will remain constant regardless of the composite output level.

The telemetry simulator provides for an engineering data channel (Fig. 7) and a science data channel (Fig. 8). The engineering data channel has bit (clock) rates of $8\frac{1}{3}$ or $33\frac{1}{3}$ bits/s. The engineering data format is a 15-bit, pseudo-noise (PN) sync word followed by a 6-bit index word that locates medium- and low-speed commutator decks during any pass of the high-speed commutator deck. The index word is followed by seventeen 7-bit words whose content is selectable by the ENGR CHANNEL switches. A central computer and sequencer (CC&S) memory readout simulation has been provided to check the CC&S mode. Also, a periodic PN generator has been provided so that PN sequences of four lengths can be substituted for the normal engineering data format.

d. Theory of operation

Engineering channel. A 480-kHz oscillator is used as the master clock source for generating all bit rates and clocks. An external oscillator may be substituted for the internal 480-kHz oscillator. The external signal, regardless of polarity, will be conditioned in the input conditioning circuit (ICC) to be compatible with the integrated circuit logic.

The 480 kHz signal is divided by 20 to form the engineering channel subcarrier frequency of 24 kHz. The subcarrier is divided by 180 to form the $133\frac{1}{3}$-pulses/s signal. The $133\frac{1}{3}$-pulses/s signal is further divided by two successive divide-by-4 counters to generate both a $33\frac{1}{3}$ and a $8\frac{1}{3}$ pulses/s signal. The pulse rate selected is determined by the state of the mode/rate generator; the actual rate selection being performed in the engineering bit-rate selector logic.

An external engineering bit sync source can be substituted for the internal engineering bit sync. The selected bit-sync signal (internal/external) is divided by 7 (bit counter) to form a word-sync pulse. The engineering

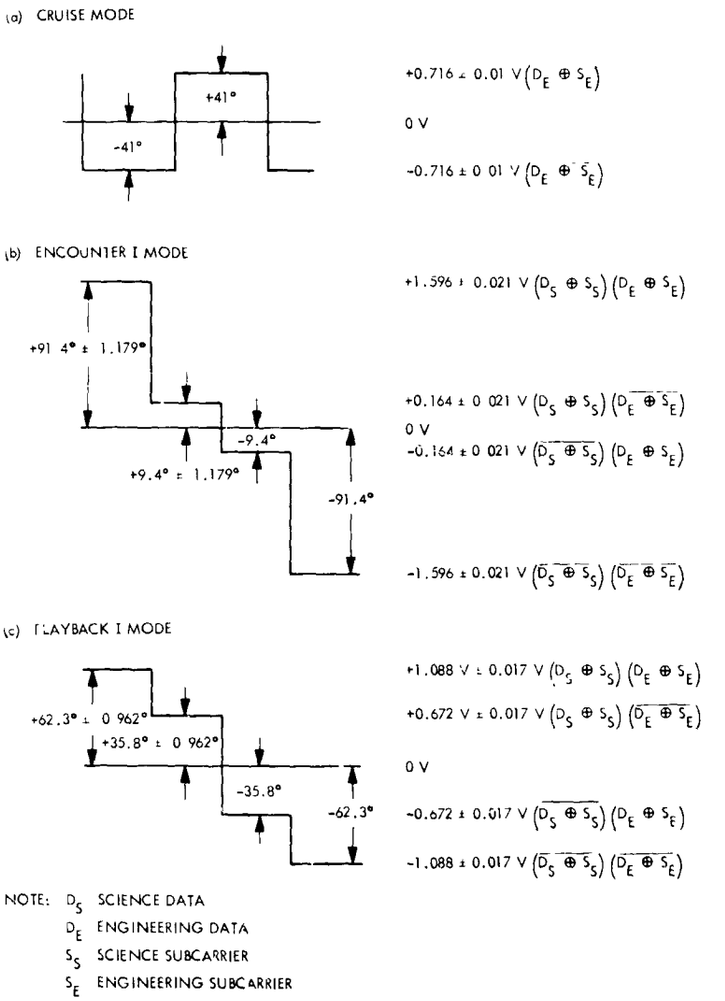

Fig. 6. Modulation algorithms

word sync is sent to a 12-μs one-shot and then to a buffer amplifier (BA). The BA output (engineering bit sync) is used as one of the data synchronization signals by the TCP. The word-sync signal is used as a clock for a divide-by-20 counter, which represents the 20 channels of the high-speed commutator deck.

The first three states of the divide-by-20 counter are decoded and used as load/transfer pulses for the commutator medium-speed deck, the CC&S data register, and the engineering data shift register. The word counter states refer to data channels in the high-speed deck: word counter state one (WCS1) is channel 100, WCS2 is channel 101, and WCS3 is channel 102. The WCS1 forms a frame start pulse that is sent through a one-shot and BA. It is also used to drive two divide-by-10 counters and one divide-by-2 counter whose states simulate decks. The states of these three counters generate a 6-bit index word that is inserted in the engineering data at channel 102 time. The index word is used by the DSIF decommutator to determine the positions of the medium- and low-speed decks in the engineering data stream.

The engineering data stream consists of the 15-bit PN sync word and the 6-bit index word. The remaining 17 high-speed words are generated from the engineering CHANNEL DATA SELECT switches.

The output from the engineering data shift register goes to the engineering data select logic. When the CC&S indicator is *off*, the engineering data shift register output is transferred to a biphase modulator. When the

CC&S mode has been selected from the CC&S mode/rate selector, the CC&S data stream is transferred through the data select logic. On the first pass of the high-speed deck after CC&S has been commanded, the CC&S data register is loaded with the CC&S index word (011111). The index word will be followed by an alternating pattern of zeros and ones, simulating CC&S memory readout data, until the CC&S selection is terminated.

The biphase modulator receives the selected engineering data and modulates the engineering subcarrier, resulting in the logic expression $(\overline{D_E\bar{S}_E + \bar{D}_E S_E})$. The modulator output is sent to the engineering data mode select logic. This logic controls the input to the mixer–modulator. If the *cruise* or *encounter I* modes are selected, the data is transferred to a particular input to the mixer. In the *playback I* mode, the data is transferred to another input to the mixer.

The engineering data is sent to a 0–3-bit delay register. The selected delayed data is transferred through a BA for use in the TCP. The data is delayed with respect to the data commutated from the composite telemetry signal.

Science channel. The 480-kHz oscillator is used to drive a divide-by-14 counter. The output of the divide-by-14 counter is the 34.286-kHz science channel subcarrier frequency. When an external oscillator is used, both the engineering and science subcarriers are derived from it.

A 259.2-kHz oscillator is used as a master clock source for generating the science channel bit rates. An external oscillator can be substituted for the internal 259.2-kHz oscillator. The external signal, regardless of polarity, will be conditioned in the ICC to be compatible with the integrated circuit logic.

The 259.2-kHz signal is fed to divide-by-3888 and divide-by-960 counters. The output of the divide-by-3888 counter forms the *encounter I* 66⅔-pulses/s bit rate. The output of the divide-by-960 counter forms the *playback I* 270-pulses/s bit rate. Outputs from both of these counters are sent to the science bit-rate selector where one of the rates is selected, depending on the state of the mode/rate generator, to become the science channel bit sync.

An external source can be selected for the bit sync instead of the internal bit rate. The selected bit sync signal is then sent to a 12-μs one-shot and then to a BA. The BA output (science bit sync) is used as one of the data synchronization signals by the TCP.

The selected bit sync is routed by a divide-by-280 counter (bit-time counter) to the science data register. Bit-time 280 is sent to a 12-μs one-shot and then to a BA, the output of which is science channel frame start. The frame-start pulse indicates to the TCP that the next 15 data pulses will be the science PN sync word.

The science data stream consists of the 15-bit PN sync word followed by 265 data pulses that compose the science data frame, which is a sequence of alternating zeros and ones.

The science data signal is transferred to the biphase modulator. The biphase modulator receives the science data and modulates the science subcarrier, resulting in the logic expression $(D_S S_S + \bar{D}_S \bar{S}_S)$. The output of the modulator is fed to the science data mode select logic. This logic controls the input to the mixer–modulator. If the *encounter I* or *playback I* modes are selected, the data is transferred to a particular input in the mixer. If *cruise* mode is selected, the science data mode select logic will inhibit the transfer of data to the mixer.

The science data is fed to a 0–3-bit delay register. The selected delayed data is transferred through a BA for use in the TCP. The data is delayed with respect to the data input to the biphase modulator and to the data decommutated from the composite telemetry signal.

e. Design characteristics

Mode/rate generator. As shown in Fig. 7, the mode/rate generator controls the modes and bit rates. The mode logic generates signals that are fed to the mixer–modulator input circuitry, to the bit-rate selectors, and to the engineering data selector. The modulator input circuitry refers to the engineering and science data mode select logic. The outputs from the data-mode selectors go to different inputs on the mixer–modulator. The inputs selected determine what modulation algorithm is to be chosen (Fig. 6). The engineering and science modulated subcarriers are linearly added in the mixer–modulator and used as an input to a differential amplifier (modulator).

PN sequence generator. The PN sequence generator generates any one of the maximum length PN periodic sequences. The PN sequences can be substituted for the

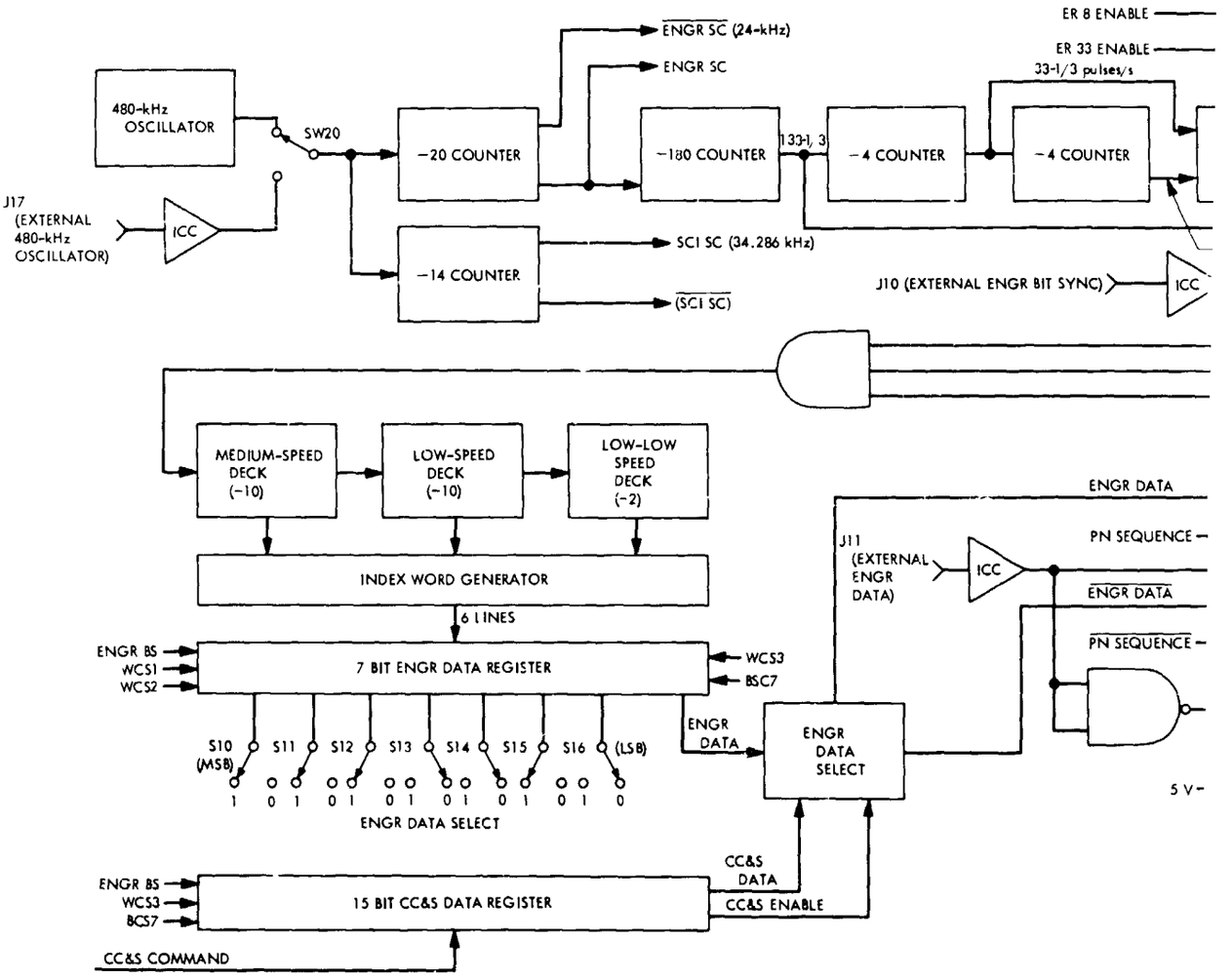

BA BUFFER AMPLIFIER
BCS BIT COUNTER STATE
BS BIT SYNC
BSC BIT SYNC CLOCK
CC&S CENTRAL COMPUTER AND SEQUENCER
D_E ENGINEERING DATA
D_S SCIENCE DATA
ENC I ENCOUNTER I
ER ENGINEERING RATE
ICC INPUT CONDITIONING CIRCUIT
LSB LEAST SIGNIFICANT BIT
M/M MIXER/MODULATOR
MSB MOST SIGNIFICANT BIT
NRZ NON-RETURN TO ZERO
OS ONE SHOT
PB I PLAYBACK I
PN PSEUDO NOISE
SC SUBCARRIER
S_E ENGINEERING SUBCARRIER
S_S SCIENCE SUBCARRIER
SW SWITCH
WCS WORD COUNTER STATE
WS WORD SYNC

FOLDOUT FRAME

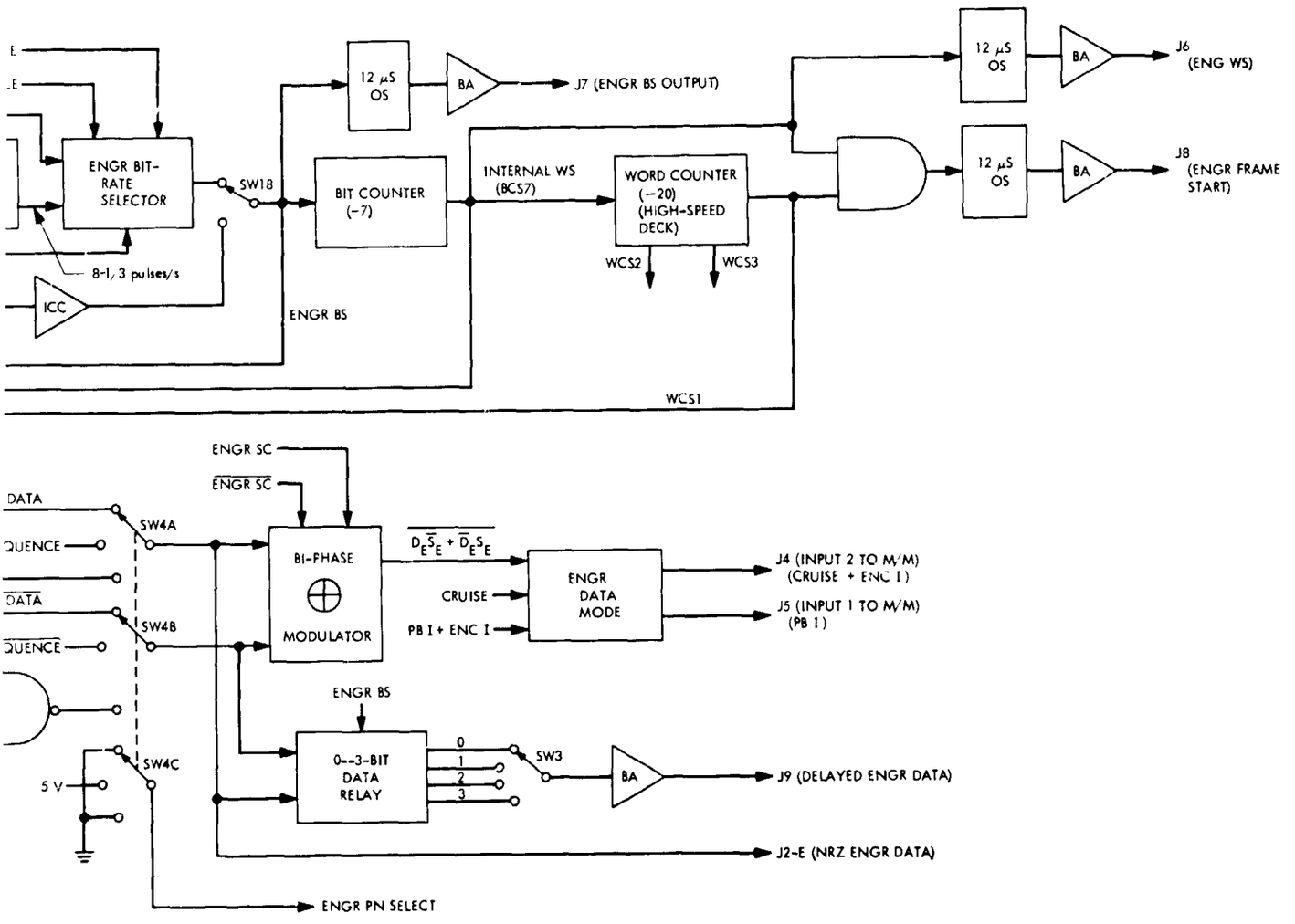

Fig. 7. Engineering data channel functional block diagram

FOLDOUT FRAME # 2

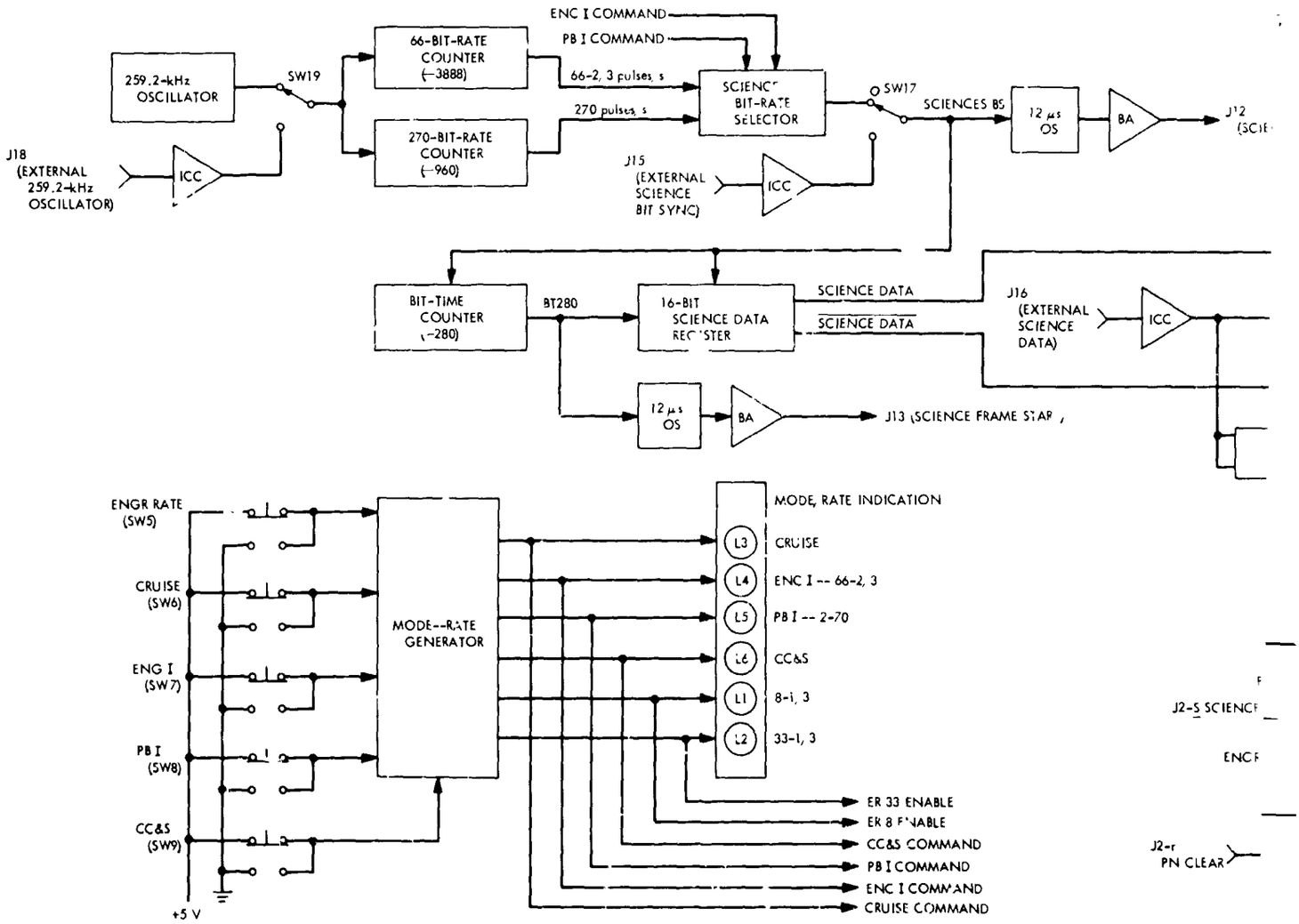

BA BUFFER AMPLIFIER
BS BIT SYNC
BT BIT TIME
CC&S CENTRAL COMPUTER AND SEQUENCER
D_E ENGINEERING DATA
D_S SCIENCE DATA
ENC I ENCOUNTER I
ER ENGINEERING RATE
ICC INPUT CONDITIONING CIRCUIT
L LAMP
NRZ NON-RETURN TO ZERO
OS ONE SHOT
PB I PLAYBACK I
PN PSEUDO NOISE
SC SUBCARRIER
S_E ENGINEERING SUBCARRIER
S_S SCIENCE SUBCARRIER
SW SWITCH

Fig. 8. Science data channel functional block diagram

FOLDOUT FRAME #1

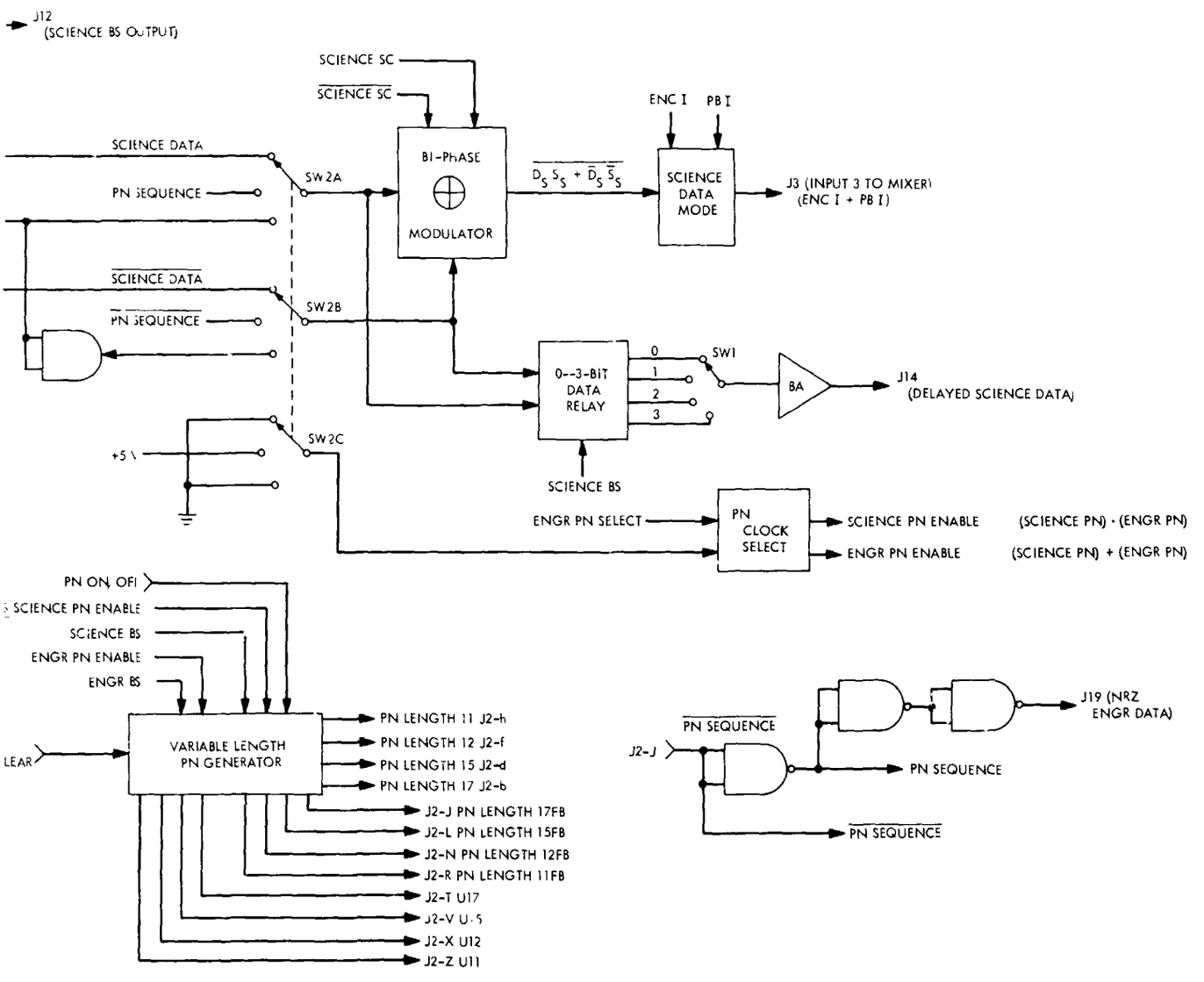

FOLDOUT FRAME FOLDOUT FRAME # 2

normal engineering or science data patterns. The generator has four selectable PN lengths. The cycles times for these lengths are given in Table 4.

Engineering integrator/amplifier. The engineering channel integrator/amplifier is composed of nine resistors, a 0.18-μF capacitor, and an operational amplifier. The nine resistors and the capacitor form the integrator, which has time constants ranging from 0.0 to 1.8 s.

The gain of the operational amplifier is determined by the loop equation

$$V_0/V_i = \left[1 + \left(\frac{R_1}{R_i}\right)\right]$$

The feedback resistor R_1, a 200-kΩ potentiometer, allows for gains from 1 to 45. The output voltage for the engineering integrator/amplifier will range from 125 mV to 5.6 V peak for an input of 125-mV peak signal.

Science integrator/amplifier. The science channel integrator/amplifier is identical to the engineering integrator/amplifier.

Composite signal generator. The composite signal generator is a mixer circuit that linearly adds the input signals from the engineering and science channels. Signal selection is based on the telemetry simulator mode. The modulator section is a very sensitive differential amplifier that receives the selected signals from the mixer, scales the inputs, performs linear addition, and provides an output to drive a 50-Ω terminated load.

Interface compatibility. The telemetry simulator experienced some interface difficulties with the DSIF equipment. One of these interface incompatibilities was the composite signal input to the subcarrier demodulator assembly. A Hewlett Packard 467A isolation amplifier and a Microlab/FXR Model AD-20-N attenuator were added to the simulator composite signal output. These provided the composite signal with a greater range of amplitude and a more compatible impedance match between the simulator and the subcarrier demodulator assembly.

Another interface incompatibility was between the FR1200/100 tape recorder and the simulator. The FR1200/100 tape recorder provides simulated data that is used to check communication links at the DSS and to verify DSS operation. The simulator accepts the FR1200/100 data and conditions it with the required subcarrier to form the composite signal. The interface incompatibility originated in the signal strength coming from the FR1200/100. The simulator will accept a signal strength of 5 V minimum (or -5 V maximum). Because the signal from the FR1200/100 was only 1.4 V maximum, a Dynamics amplifier 6122 was added to the MDE rack to amplify the FR1200/100 signal to be compatible with the simulator input requirement.

Both the engineering and science integrated data required a Dynamics amplifier 6122 to increase their range of amplitude. Both of these signals interface with the TCP. When the longer time constants for the integrated data are used, the amplitude of the signal decreases. The Dynamics amplifier aids in amplifying the signal to the TCP.

f. Conclusion. Installation of all six telemetry simulators has been completed and each piece of equipment has been in operational use for several hundred hours. The first unit was installed in the JPL Compatibility Test Area (Building 125-B14). The equipment has performed satisfactorily during 8 mo of continuous operation (24 h/day).

Two sets of complete documentation have been provided for each unit. Spare printed circuit boards have also been provided and the Goldstone Depot has an extra set of spare printed circuit boards and discrete component spares as well as a complete set of documentation.

Table 4. Cycle times for selectable PN lengths and various bit rates

Length	Cycle time for indicated bit rate			
	8⅓ bits/s	33⅓ bits/s	66⅔ bits/s	270 bits/s
2047	$0^h\ 4^m\ 5^s$	$0^h\ 1^m\ 1.4^s$	$0^h\ 0^m\ 30.7^s$	$0^h\ 0^m\ 7.6^s$
4094	$0^h\ 8^m\ 12^s$	$0^h\ 2^m\ 3^s$	$0^h\ 0^m\ 41.4^s$	$0^h\ 0^m\ 15.2^s$
32,767	$1^h\ 5^m\ 21^s$	$0^h\ 16^m\ 23^s$	$0^h\ 8^m\ 11^s$	$0^h\ 2^m\ 1^s$
131,071	$4^h\ 21^m\ 30^s$	$1^h\ 5^m\ 32^s$	$0^h\ 32^m\ 48^s$	$0^h\ 8^m\ 6^s$

E. Guidance and Control

1. Attitude Reference and Star Identification Program

The IBM 7094 computer programs, Attitude Reference Program for *Mariner* (ATRM) and Star Identification Program for *Mariner* (SIPM), described in SPS 37-51,

Vol. I, p. 13, have been completed and certified operational for the *Mariner* Mars 1969 missions. Final documentation for both programs is scheduled to be completed by March 15, 1969.

The capability of SIPM to provide star maps [simulations of the responses of the Canopus sensor to light stimuli (i.e., stars, planets, and background) in the field of view of the Canopus sensor] during a midcourse maneuver enables the current version of SIPM to provide information not available from previous versions of SIPM. First, star maps now may be obtained for turns about the pitch axis (previously, star maps could be obtained only for turns about the roll axis). Second, star maps may be obtained for turns about an axis aribitrarily oriented with respect to the sun–probe–Canopus coordinate system. This latter capability is particularly important in identifying acquirable objects when and if the spacecraft acquires a fixed, non-standard orientation with respect to the sun–probe–Canopus coordinate system.

The star maps provided by the current version of SIPM may also be used as an aid in gaging the accuracy with which events such as sun acquisition and midcourse maneuver turns are completed.

F. Space Sciences

1. Data Automation Subsystem Testing

The first phase of the *Mariner* Mars 1969 data automation subsystem (DAS) testing sequence was conducted at the contractor's[6] facility under JPL supervision. The initial checkout was performed at the subassembly level. Fabrication errors were corrected and marginal integrated circuits (IC) were replaced during the subassembly test phase. Each of the DAS units was completely assembled and tested in accordance with an acceptance test procedure. Separate test procedures existed for subassembly and subsystem testing. Manually-operated bench checkout equipment (BCE) consoles, also fabricated at the contractor's facility, were utilized to perform the subsystem-level tests prior to delivery to JPL. These tests were conducted under worst-case conditions, i.e., ±10% of the nominal voltage at the ambient −10 and +65°C temperature environments. This procedure distinguished temperature-sensitive components that were replaced. When the units successfully completed the temperature cycle tests, they were delivered to JPL. The BCE consoles were tested with the DAS breadboard prior to testing a flight unit. Also, all BCE consoles were delivered to JPL to support environmental and subsystem-level testing.

Upon delivery to JPL, each DAS completed a more comprehensive voltage–temperature margin test using a Digital Equipment Corporation Programmed Data Processor-7 (PDP-7). The computer test system controlled the input data to the DAS and continuously monitored all DAS outputs. Processing of the data was accomplished in real time, thus providing a complete functional test that enabled the detection of design problems not previously discovered during manual testing. The software was developed at JPL and provided an error printout capability. Each DAS was tested in accordance with a JPL test procedure written specifically to test the *Mariner* Mars 1969 DAS. A portion of this test procedure (JPL TP504466) specified that the nominal operating voltage (+4.0 V) be decreased until the DAS failed to operate. Each "fail point," where a function ceased to operate, was measured within 5 mV and documented. Finally, the "gross fail point" was reached which would conclude that portion of the test. Table 5 shows the first fail point and the gross fail point of the three flight units.

The voltage–temperature margin data from each unit was analyzed and used as a reference for evaluating subsequent margin test results. A comparison was made between the data from each test and between different units. This provided a mechanism for a complete detailed evaluation of each system. Changes in fail point trends may be indicative of marginal components. The margin tests were used to establish the high level of confidence required for flight hardware and to ensure

Table 5. First and gross fail points of three DAS flight units[a]

Temperature, °C	Flight unit 1		Flight unit 2		Flight unit 3	
	First fail point	Gross fail point	First fail point	Gross fail point	First fail point	Gross fail point
Ambient	2.725	2.685	2.740	2.700	2.725	2.700
−10	2.990	2.925	3.005	2.955	3.010	2.985
+65	2.625	2.455	2.495	2.400	2.665	2.440

[a]Normal V_{cc} = +4.0 V.

[6]Litton Industries, Inc., Guidance and Control Systems, Woodland Hills, Calif.

a high probability of exposing marginal conditions before they become malfunctions.

After completion of these tests, the units were flight-acceptance tested at the JPL environmental facilities and then returned to the computer test system for another complete voltage–temperature margin test. The flight units were then delivered to the Spacecraft Assembly Facility (SAF). Prior to SAF delivery, the three flight units had accumulated a combined total of 4523.9 h of testing (1634.8, 1401.4, and 1487.7 h on flight units 1, 2, and 3, respectively).

This test sequence has significantly reduced the probability of a system fault. It also provides the capability to analyze spacecraft-system-oriented problem areas.

II. *Mariner* Mars 1971 Project

PLANETARY–INTERPLANETARY PROGRAM

A. Introduction

1. Mission Description

The primary objective of the *Mariner* Mars 1971 Project is to place two spacecraft in orbit around Mars that will be used to perform scientific experiments directed toward achieving a better understanding of the physical characteristics of that planet. Principal among these experiments are measurements of atmospheric and surface parameters at various times and locations to determine the dynamic characteristics of the planet. Approximately 70% of the Martian surface will be observed during a minimum of 90 days of orbital operations.

During Mission A, it is planned to map the topography of a large portion of the Martian surface at a resolution significantly higher than that achievable with earth-based methods or by the *Mariner* Mars 1969 spacecraft. In addition, measurements will be made of the composition, density, pressure, and thermal properties of the planet's atmosphere. Other measurements will be directed toward an understanding of Mars' surface temperatures, composition, and thermal properties (particularly at the polar caps); its apparent lack of internal activity, its mass distribution; and its shape.

During Mission B, data will be sought on time-variable features of the Martian surface associated with the wave of darkening wherein both seasonal and secular changes occur. Also, information on atmospheric structure and gross dynamics will be obtained, as well as information directed toward an understanding of Mars' mass distribution, its shape, and its apparent lack of internal activity.

A capability will exist to redirect goals for either mission to the alternate mission if desired. The two launches are anticipated for May 1971, with arrival at the planet during the following November.

An engineering objective of the project is to demonstrate the ability of the spacecraft to perform orbital operations in an adaptive mode wherein information from one orbital pass is used to develop the operations plan for subsequent orbital passes. If sufficient resources are available, the necessary modifications will be made to extend the useful lifetimes of the spacecraft past the required 90 days.

One of the *Mariner* Mars 1971 flight spacecraft will be new, and the other will be the spare flight spacecraft of the *Mariner* Mars 1969 Project modified to meet the requirements of the 1971 missions and to enhance mission

reliability. The proof test model spacecraft of the *Mariner* Mars 1969 Project will be modified to become the proof test model for the *Mariner* Mars 1971 Project, to be used for preliminary testing and as a simulator in support of flight operations. A major modification for the *Mariner* Mars 1971 mission will be the addition of a rocket motor required to decelerate the spacecraft and place it in orbit around Mars. The spacecraft configuration is shown in Fig. 1.

Separate scientific instrument subsystems will be required to accomplish each of the first seven planned scientific experiments given in Table 1. The S-band occultation and celestial mechanics experiments will require no additional equipment on the spacecraft. Measurements will be made during both the orbital and the cruise phases of each mission.

Management responsibilities for the overall project, the Spacecraft System, the Mission Operations System (MOS), and the Tracking and Data System (TDS) have been assigned to JPL. Lewis Research Center has been assigned management responsibility for the Launch Vehicle System (LVS). The launch vehicle will be an *Atlas/Centaur* developed by General Dynamics/Convair.

The *Mariner* Mars 1971 missions will be supported by the Air Force Eastern Test Range launch facilities at Cape Kennedy, the tracking and data acquisition facilities of the Deep Space Network, and other NASA facilities.

Table 1. *Mariner* Mars 1971 scientific experiments

Experiment	Principal scientific investigator	Affiliation
Television	H. Masursky[a]	U.S. Geological Survey
	G. de Vaucouleurs	University of Texas
	J. Lederberg	Stanford University
	B. Murray	CIT
	W. Thompson	Bellcomm
Infrared radiometer	G. Neugebauer	CIT
Ultraviolet spectrometer	C. Barth	University of Colorado
Infrared interferometer spectrometer	R. Hanel	Goddard Space Flight Center
Charged-particle telescope	J. Simpson	University of Chicago
Dual-frequency receivers	V. Eshleman	Stanford University
X-ray particle detector	J. Van Allen	University of Iowa
S-band occultation	A. J. Kliore	JPL
Celestial mechanics	J. Lorrell[a]	JPL
	I. Shapiro	MIT

[a]Team leader.

2. Project Status

The mission design review was concluded on January 31, 1969. As a result of the review, some changes are being made to the draft of Part I of the Mission Specification and Plan. The memoranda of agreement for science principal investigators are being prepared, reviewed, and signed off by the principal investigators and the *Mariner* Mars 1971 Project.

The Spacecraft System functional design, approximately 95% complete, was reviewed on February 20–21, 1969. The interface definitions between spacecraft subsystems, including science instruments, are being concluded in order to permit a timely completion of detailed spacecraft design.

The MOS/TDS management plan has been issued and special emphasis is now being placed on the early definition and implementation of simulation system requirements. Mission alternates are the subject of continuing analyses.

The TDS simulation and monitor systems definitions have been completed. The *Mariner* Mars 1971 Project's flight-path operations computer support will be provided by TDS on the 1108 computer.

B. Telecommunications

1. Magnetic Tape Station Studies

a. Introduction. One problem in the use of reel-to-reel magnetic tape recorders for spacecraft data storage is the phenomenon of layer-to-layer separation occurring in a tape pack (reel of tape wound and stored under tension) when it is subjected to wide temperature transients. Layer-to-layer separation may occur at various radii within the pack accompanied by a loss of tape tension in those areas. Associated with this loss of tension in certain areas is an overstressed condition in other areas resulting in an increase in pressure between adjacent layers of tape. These phenomena are caused by an apparent inability of the wound magnetic tape to adjust itself evenly throughout the pack during expansion and contraction. Such conditions frequently result in permanent damage to the tape also and threaten the integrity of transport operation to some degree, depending upon the concept of tape reeling and guidance employed.

(a)

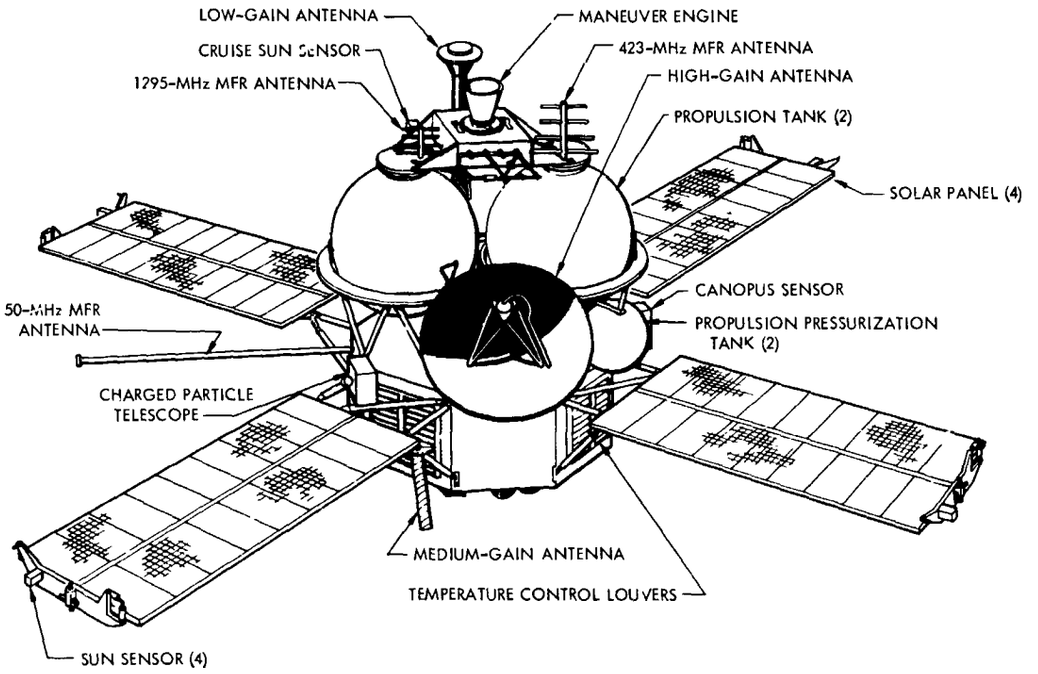

NOTE: PROPULSION MODULE INSULATION BLANKET NOT SHOWN
MFR = MEDIUM-FREQUENCY RECEIVER

(b)

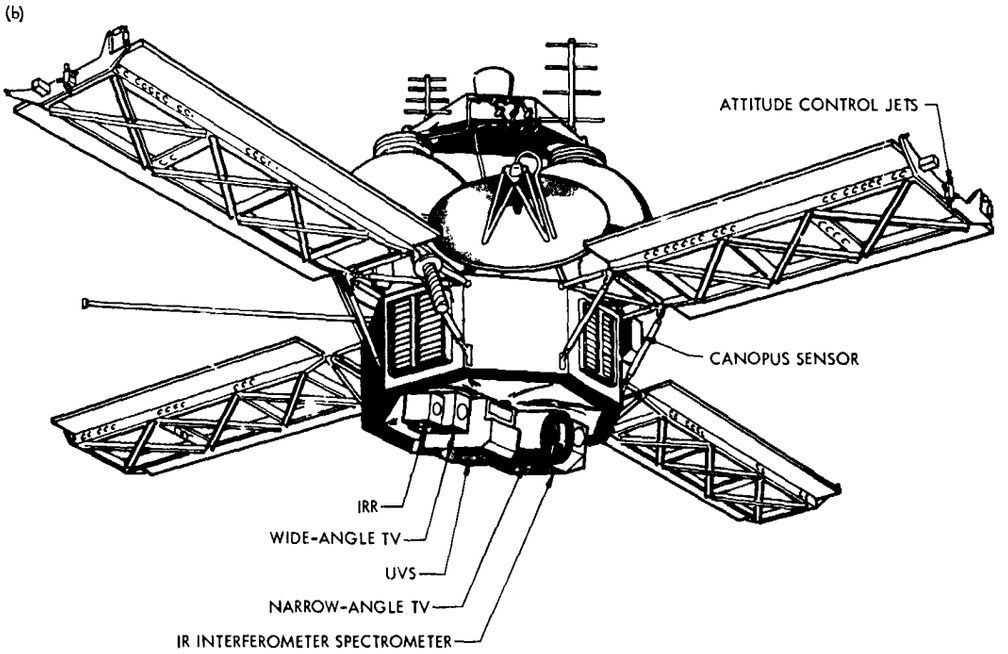

Fig. 1. *Mariner* Mars 1971 spacecraft configuration: (a) top view, (b) bottom view

One effect of separation at any point is to permit lateral shifting of one or more circumferential wraps of tape. This would be of particular concern when the pack is under the influence of external shock or vibration forces. In the absence of retaining elements, such as reel flanges or a peripheral pressure belt, these influences could cause the loss of the entire pack. Where retaining elements are provided, their guiding effect may result in severe edge damage and/or folding at points of contact with the tape during operation. In either case, the loss of data or storage capability could be catastrophic.

A second significant effect is introduced by the resultant variation in tape tension throughout the pack. This is manifested as a non-uniform rate of tape travel across the magnetic heads during transfer from one reel to the other, causing signal inconsistencies during recording and playback.

In areas where excessive inter-layer pressure exists due to abnormally high tape tension, permanent distortion of the tape is likely to occur. The result is lateral cupping of the tape and/or rippling of its edges. Damage of this nature causes serious tape tracking problems and loss of head-to-tape contact. High inter-layer pressure, in conjunction with exposure to elevated temperatures, also contributes to layer-to-layer adhesion or "blocking". The characteristics of this particular phenomenon have been investigated previously and are discussed in SPS 37-42, Vol. IV, pp. 176–178.

The functional performance characteristics of any spacecraft data storage subsystem, and the techniques established to achieve them, are significantly dependent upon the capabilities of the storage medium. Therefore, in the case of the tape recorder, it is essential that the integrity of the magnetic tape be preserved throughout the mission. Recognizing the above mentioned as some of the problems associated with tape recorder use in the spacecraft environment, a program was undertaken to investigate its limitations and recommend means of overcoming them to meet future spacecraft data storage requirements.

b. Background. Typically, the magnetic tape recorder system is not operated during the long cruise periods of spacecraft planetary missions. This is desirable for various reasons; however, in consequence, it is during these periods that the tape pack is most vulnerable to the effects of environment extremes. During 1968, the engineering test model (ETM) tape transport,[1] a prototype isobelt-drive machine, was employed as a test vehicle to determine the ability of such a system, including the magnetic tape pack, to survive a *Mariner* type-approval level test program.[2]

During the vacuum–temperature test phase, characteristics of tape pack instability were observed that are now understood to be typical. A range of temperature change was imposed with the cycle starting at room ambient temperature, dropping to −20°C, soaking for 24 h, rising to 75°C, soaking for eight days, and dropping again to ambient. Temperature transients were performed with the transport non-operating and one tape reel full. Visual observations were made and system operational performance was checked at each stabilization temperature. No pack separation was apparent at low temperature until the machine was operated. During operation, a tendency for layers of tape near the outside diameter of the supply reel to separate and create a gap in the area of isobelt tangency was noted. Several reversals of direction seemed to eliminate the condition temporarily at any particular point. However, tracking became marginal and the tape threatening to walk off the reel at one pont. After stabilization at high temperature, the separation that developed at low temperature disappeared; however, new gaps were evident at various radial points within the full pack, particularly near the hub. Significant performance degradation after thermal exposure tests suggested tape damage and pack instability. This was verified during subsequent attempts to operate the transport at ambient conditions. Continued operation became impossible due to mistracking. Examination of the tape revealed severe cupping and edge distortion.

The test experience, coupled with information obtained from magnetic tape experts and tape recorder manufacturers, prompted further investigation of the tape stability problem. The studies were also encouraged by project groups due to the need for information applicable to future mission data-storage requirements.

c. Program definition. Two classes of tests were established: static (non-operating) and dynamic. The static tests were designed to observe and evaluate tape pack physical condition throughout a temperature range and

[1] *Improved Magnetic Tape Recorder*, Oct. 1966 (JPL internal document).

[2] *Type Approval and Flight Acceptance Test Requirements, Mariner Mars 1969 Flight Equipment*, Dec. 13, 1967 (JPL internal document).

under physical installation conditions simulating those of a typical reel-to-reel tape transport. Eighteen different tape types from six manufacturers have so far been tested in an effort to ultimately determine the best tape, from a physical standpoint, presently available for spacecraft application.

The dynamic test consisted of operating the tape transport during temperature change, and allowing it to soak non-operating at the extremes. This was done to assess the ability of the tape pack to adjust to thermal stresses while moving during temperature transients, thereby avoiding damage due to unrelieved stresses during static soak.

Performance tests were conducted and all tapes were visually examined before and after thermal exposure. The environmental chamber was controlled to obtain a temperature change rate of 30°C/h. A fixture previously designed for another study effort (SPS 37-42, Vol. IV) was used to support the tape packs in tension as wound while under test (Fig. 2). A 4-oz weight attached to the free end of the pack supplied constant tension. Since the ETM transport was employed as a performance test vehicle throughout the investigation, the reel hub and tape pack diameters adaptable to that machine were used (1.250 and 3.125 in., respectively).

d. Test results

Static tests. A summary of the static test data taken to date over the range of −20 to 75°C is shown in Table 2. All tapes listed are ½-in. wide and have a polyester backing. The various binder formulations are unknown.

It is interesting that most of the tapes showed signs of separation during or after the high-temperature soak, and most of those during the rise from −20° to ambient. There is also a pronounced corelation, among all tapes, of the radii of the points in the pack where separation occurs.

Some capability of self-adjustment to temperature reduction was visible in the three Consolidated Electrodynamics Corporation (CEC) sample tapes as evidenced by an evenly distributed inter-layer slippage. Figure 2 illustrates this characteristic. In this experiment, each tape pack was initially marked with a straight radial white line as it appears on the right-end pack in Fig. 2. Impending inter-layer separation resulting from contraction of tape within the pack was pre-empted, in varying degree with different tape samples, due to inter-layer

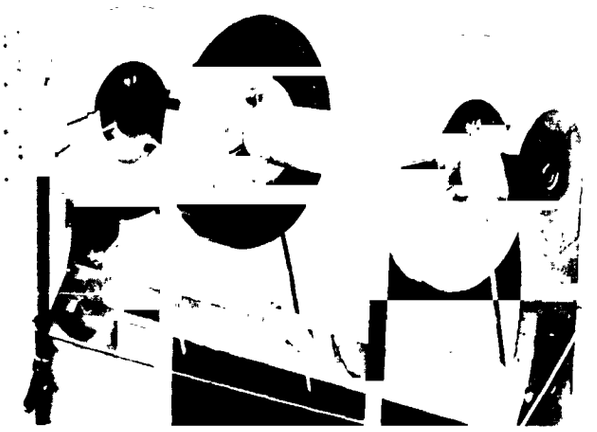

Fig. 2. Tape packs mounted for thermal exposure

slippage. The center pack (CEC W-1) appeared to be the most consistent in this respect. Note the involute shape of the marking, which indicates evenly distributed adjustment. The tape pack at the left end of the fixture [Minnesota Mining and Manufacturing (3M) MT22760], a lubricated tape, showed some signs of adjustment, but certainly much less than might have been expected. The 3M LR1353 sample, another lubricated tape (not shown), showed none. For the most part, all other tapes behaved very much like the right-end pack, exhibiting little or no tendency to close the gaps. It is significant that any ability to adjust at the initial low temperature is apparently of no value during subsequent exposure to high temperature. In fact, examination of the data would seem to indicate a more severe final condition of layer-to-layer separation with those tapes exhibiting greater slipping tendencies. In this regard, some previous investigations into the dimensional characteristics of magnetic tape, when subjected to variations in temperature,[1] may be pertinent. The results suggest that certain irreversible dimensional changes that vary with time and stress may, in some cases, make a tendency for inter-layer slippage undesirable. Variation in stress in areas where inter-layer separation does occur may permit localized tape shrinkage at elevated temperatures, resulting in at least some degree of gap closure.

During performance testing on the transport after completion of the thermal cycle, all tapes exhibited some tendency for the outer layer to adhere to the pack during

[1] *Thermal Shrinkage of Polyester-Base Magnetic Tape*, Jan. 1966 (JPL internal document).

Table 2. Static test data tabulation

Tape type	Location of layer-to-layer separations (pack radius), in.					
	25 to −20°C	24-h soak at −20°C	−20 to 75°C	24-h soak at 75°C	75 to −20°C	−20 to 25°C
3M 999	None	NC	NC	NC	1.3	NC
3M 551	None	NC	NC	NC	NC	0.9, 1.3
3M 951	None	NC	NC	NC	NC	0.9, 1.3
3M 154	None	NC	NC	0.9, 1.1	NC	RC
3M MT22760 (lubricated)	None	SA	NC	0.9, 1.1	NC	1.1, 1.3
3M 1R1353 (lubricated)	None	NC	NC	NC	0.9, 1.3	0.9, 1.1, 1.3, 1.4
DuPont Crolyn	None	NC	NC	NC	0.9, 1.1	0.9, 1.5
Ampex 746	None	NC	1.3	NC	NC	0.9, 1.3
Ampex 748	None	NC	1.0	NC	NC	1.0, 1.5
CEC M-1	None	SA	0.9	NC	0.9, 1.1, 1.3	0.9, 1.1, 1.3, 1.4
CEC SX-1	None	SA	NC	NC	NC	0.9, 1.1
CEC W-1	1.3	SA, RC	NC	NC	0.9, 1.1, 1.3	0.9, 1.1, 1.3, 1.4
Soundcraft 2HRMB/B	None	NC	1.3	NC	NC	1.1, 1.3
Soundcraft 2HRM	None	NC	NC	NC	NC	0.9, 1.1, 1.4
Memorex 33B	NC	NC	NC	NC	NC	1.1
Memorex 53A	1.1	NC	NC	1.4	NC	RC
Memorex 62L	None	NC	NC	0.9, 1.3	NC	1.2 1.3
Memorex 63L (high temperature)	None	NC	NC	1.3	NC	NC

NC = no change from previous condition
SA = self-adjusted through inter-layer slip
RC = returned to original condition

unwinding (SPS 37-42, Vol. IV). This occurred in varying degrees and uniformity with each case. The Memorex samples, with the exception of 63L tape (designed for high-temperature applications), exhibited the most severe adhesion. Oxide was actually stripped off at some points indicating blocking. Generally, the 3M tapes performed the best in this respect, although all tapes showed some signs of stacking inconsistency and potential tracking problems after thermal exposure. All of the Memorex tapes, in particular, exhibited considerable tendency to distort to the extent that it was impossible to properly track the tape.

Dynamic tests. Three different types of tape were selected for preliminary operational tests on the ETM transport during temperature cycling. The 3M 551 sample was used because it appeared to have desirable characteristics of signal record and reproduction, making it a likely candidate for *Mariner* Mars 1971 mission application. Samples of this tape were run to two high temperature extremes: 75 and 55°C. The second test at 55°C was performed to assess the possibility of avoiding tape-to-head sticking, which did occur during the soak period at 75°C. A run using the 3M 999 sample was made to provide data for evaluation, relative to previous experience with the ETM, while undergoing *Mariner* type approval environmental testing. A fourth run was made using Memorex 63L high-temperature tape. This was done to qualify or substantiate the results of the static tests on this tape.

Observations of the tape stacking and tracking throughout the first three test runs revealed no irregularities in tape winding. The tape seemed to adjust to the change in temperature, with no apparent damage, even during the soak periods. However, during the first test using the 3M 551 tape, the tape stuck to the heads while soaking at 75°C. This sticking was serious enough to destroy the tape oxide and binder layer and prevent tape motion across the heads. Figure 3 illustrates this condition. The area shown vertically and bounded on each side by horizontally oriented globules is the area of head-to-tape contact. The horizontal narrow line discolorations, which appear to run between the globules, are scars parallel to the length of the tape where binder and oxide material have softened and migrated to the edges of contact. Note that this scaring, and the associated buildup of binder and foreign matter, occurred only at locations where the tape was in contact with the brass head bracket material. The significance of this is not yet clear, but the problem did not occur when the upper temperature limit was reduced to 55°C. Sticking did not occur with either of the other two tapes at 7 °C, although the 3M 999 tape did show a possible softening of the binder at points of head contact.

During the fourth test, using the Memorex 63L tape, tracking became progressively more erratic. At the higher temperatures, the tape pack became especially irregular, and what appeared to be flat areas developed on the circumference. Several gaps gradually formed near the tape hub (Fig. 4). Note the irregular circumference, edge damage, and buckled internal layers. The tracking instability was characterized by a tendency for the tape to twist back and forth (wobble) at various points across the tape path. Twisting on the reel hub eventually forced stoppage of the transport due to imminent failure.

e. Conclusions. The discussion in this article relates only to the first phase of the program to investigate the characteristics and limitations of magnetic tape in the spacecraft environment. The results presented are preliminary in nature, the data not having yet been thoroughly evaluated, and, at this point, should be considered only as guidelines and a basis for further study. It should be noted that the CEC tapes tested are no longer being manufactured.

Another factor that should be considered in the evaluation of these, or any subsequent test data, is the possible significance of tape age or batch variations. There is some evidence that the performance of tape samples having the same identification number often varies from batch to batch. Most of the foregoing tests involved single batch samples, some of which were not recently procured.

Some tests bear repeating for sake of statistics and some tests are currently being conducted to supplement and substantiate data already obtained. Additional tests are designed to investigate various other aspects of the tape integrity problem. In subsequent phases of the study program it is planned to conduct the following types of investigations:

(1) Studies of the effects of physical and chemical changes encountered during environmental testing.

(2) Evaluation of tape pretreatment techniques.

(3) Experimentation involving various hub-diameter to tape-pack-diameter ratios.

(4) Combined thermal and physical environment tests to study the effect of vibration and shock on tape-pack-diameter ratios.

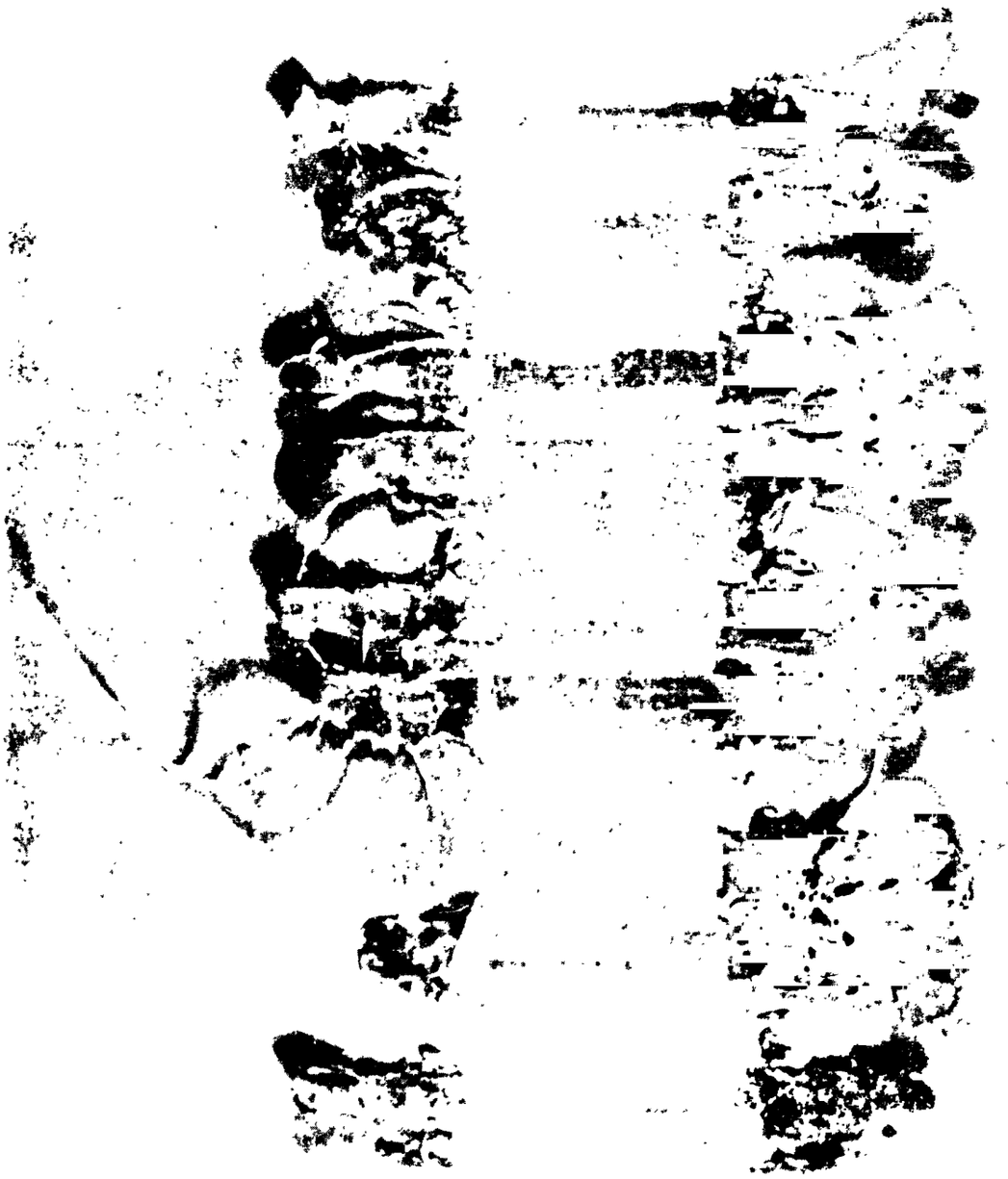

Fig. 3. Tape damage caused by adherence to magnetic head

Fig. 4. Tape pack installed in tape transport during temperature cycling

(5) Studies of head/tape interface characteristics involving the "stick–slip" phenomenon.

(6) Determinations of head and tape wear characteristics.

(7) Investigations of head design and tape guidance techniques.

These investigations will involve the testing of additional tapes having various tape backing materials and oxide/binder formulations and techniques.

From the knowledge so far obtained, only one specific conclusion can be reached. Of those tapes tested, none can be considered a reliable off-the-shelf candidate to meet the *Mariner* Mars 1971 data storage subsystem environmental requirements and performance criteria as they are now understood.

C. Guidance and Control

1. Partial Attitude Control Logic Mechanization Incorporating the Usage of a Stray-Light Detector

a. Introduction. The *Mariner* Mars 1971 mission presents several new constraints on the performance of the attitude control subsystem. This article describes one of these constraints. The periodic presence of a lighted limb in the Canopus sensor stray-light field-of-view precludes the usage of the sensor for roll control during these times. A possible logic mechanization designed to deal with these circumstances is discussed herein.

b. Stray light condition during the planetary orbit mode. Two spacecraft launchings in 1971 are postulated. The spacecraft are to orbit Mars for a period of 3 mo or more. One of the spacecraft is to assume an 80-deg angle-of-inclination orbit; the other a 60-deg angle-of-inclination orbit. Studies performed show that in the 80-deg angle-of-inclination orbit, the lighted limb of the planet appears in the Canopus stray-light field-of-view (CSFOV) for a segment of each orbit. This condition invalidates the Canopus sensor output and, under some conditions, the loss of contrast due to lighting of the background can cause the loss of Canopus acquisition (CA $1 \rightarrow 0$). In the 60-deg angle-of-inclination orbit, the planet limb may cause a false CA during the post-trim maneuver reacquisition sequence.

The attitude control electronics (ACE) logic design assumes the presence of a stray-light (SL) sensor with a logic-level type output and a field-of-view slightly overlapping the CSFOV. The two outstanding constraints placed on the ACE logic by the stray light condition (SL = 1) is that when in the normal orbital mode (Canopus acquired), when SL goes from 0 to 1 the roll control is to be switched from the Canopus sensor to the roll gyros in inertial mode. Since the presence of SL can cause a loss of CA, and since normally the absence of CA in the presence of a sun-gate signal implies roll search, the logic must discriminate against putting the system into roll search for this condition. Conversely, when the system is doing an automatic reacquisition and is in the roll search mode, the presence of stray light can cause an erroneous CA signal to terminate the roll search at an improper time. In this case also, logic must be developed to preclude that condition.

This problem is partially handled by the generation of what will be referred to as a pseudo Canopus-acquisition (PSUCA) signal. Table 3 is a truth table describing PSUCA. The no-change terms in PSUCA imply that a unit with a memory is required. A flip-flop as shown in Fig. 5 will be used. The truth table for this flip–flop is presented as Table 4, where it may be seen that by

Table 3. PSUCA truth table

CA	SL	PSUCA
0	0	0
0	1	No change
1	0	1
1	1	No change

Table 4. Flip–flop truth table

A	B	Q1	Q2
0	0	1	1
0	1	1	0
1	0	0	1
1	1	No change	No change

Table 5. Circuit truth table

CA	SL	PSUCA	A	B
0	0	0	1	0
0	1	No change	1	1
1	0	1	0	1
1	1	No change	1	1

renaming Q1, PSUCA, a new truth table (Table 5) can be written relating CA, SL, A, B, and PSUCA.

From Table 5, the following logic equations can be written:

$$\overline{A} = CA \cdot \overline{SL}$$

or

$$A = \overline{CA} + SL$$

$$\overline{B} = \overline{CA} \cdot \overline{SL}$$

$$B = CA + SL$$

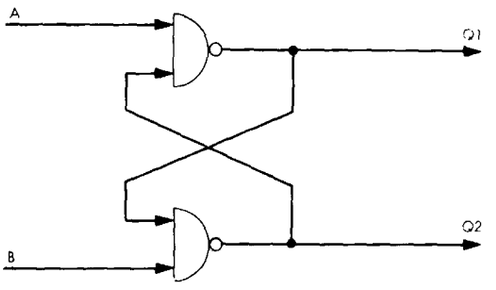

Fig. 5. PSUCA flip–flop

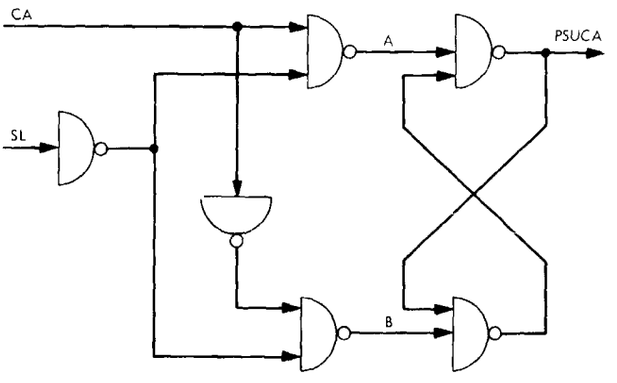

Fig. 6. Mechanized circuit

With the constraint that *nand* gates only are to be utilized, the circuit can be mechanized as shown in Fig. 6. The circuit has the property of not allowing PSUCA to change state in the presence of SL.

III. *Viking* Project, Orbiter System and Project Support

PLANETARY–INTERPLANETARY PROGRAMS

A. Introduction

The primary objective of the *Viking* Project is to send two vehicles to the planet Mars to perform scientific experiments directed toward enhancing current knowledge about the physical characteristics of the planet, particularly its capability for supporting life and possible evidence of life. The two vehicles, each consisting of an orbiter system and a lander system are anticipated for launch during 1973.

The orbiter system, to be developed by JPL, will transport and inject the lander system at the appropriate point for a selected landing site and will relay telemetered data from the lander to earth. Scientific instruments on the orbiter will be used to measure atmospheric and surface parameters at various times and locations to determine the dynamic characteristics of the planet. The topography of Mars will be mapped during orbital operations, with special emphasis on mapping the proposed landing site prior to deorbit of the lander system. Both visual and infrared coverage will be possible during the planned 90 days of orbital operations.

The lander system will be developed by Langley Research Center, which also has overall project management responsibility. During entry and after landing, the scientific instruments on the lander will measure Mars' atmospheric composition, temperature, pressure, and density. After landing, the topography of the landing site will be mapped, and measurements will be made of the planet's surface composition, temperature, pressure, humidity, and wind speed. Of particular interest in the surface measurements are the type of organic compounds present, if any, and the amount and form of water. The two scientific instruments to be used for these measurements—a gas chromatograph/mass spectrometer, for measuring both atmospheric and surface composition, and an aluminum-oxide water detector—are being developed by JPL. The surface soil analyses will be directed at detecting evidence of growth and/or metabolism.

B. Space Sciences

1. Gas Chromatograph/Mass Spectrometer Data Analysis

a. Introduction. At present, the gas chromatograph/mass spectrometer (GC/MS) is one of the most powerful analytical devices available to the scientist. A concomitant feature of this power, however, is the very large amount of data resulting from each sample analysis.

For example, a gas chromatograph effluent might contain on the order of several hundred peaks, each of which would result in a mass spectrum having on the order of one hundred peaks. If each peak is quantized to, say, 3–10 bits, one sample would produce on the order of 10^5 bits of data.

For landed capsule applications in which the total number of bits available for transmission is limited, data compression becomes a factor of significance. A study has begun to investigate various aspects of the data problem, particularly as related to a proposed pyrolysis–GC/MS experiment.[1] To date, the mass-spectrometer data study has focused on the following areas:

(1) A review of the mass spectrometry literature.

(2) The development of a library of mass spectra on digital magnetic tape.

(3) The development of computer programs to investigate the data compression properties of mass spectra.

(4) The development of computer programs to automatically identify mass spectra.

The first goal of the study is to accumulate a library of mass spectra of the compounds that might be expected to occur as cracking products from the pyrolysis–GC/MS experiment. This library would serve as the mathematical model of the data anticipated from the mass spectrometer. The effectiveness of various data compression and identification algorithms is to be tested using these data.

b. Literature review. An overwhelming abundance of literature concerning mass spectrometry is currently available. The last biennial review in *Analytical Chemistry* (Ref. 1) cited 1608 references. Many of these are concerned with data acquisition and the subsequent computer processing of mass spectral data. (An excellent review of this area has recently appeared in Ref. 2.) Data compression aspects of the problem, however, have received virtually no attention, since studies to date have been directed toward earth-based systems using large computers (Ref. 3).

c. Mass-spectra library. The library of mass spectra to be used in this study was processed as shown in Fig. 1. The two primary sources of spectral data to date have been a library of 1967 spectra published by the Dow Chemical Co. (DCC) and a library made available to us by Prof. K. Biemann of MIT (2004 spectra). An additional library of approximately 500 spectra, furnished by the Mass Spectrometry Data Center (MSDC) in England, is now being processed. A library of approximately 2000 compounds collected by the American Petroleum Institute (API) is expected to be available shortly.

For the purposes of this study, the spectral library has been divided into two categories:

(1) Category I. Those compounds which might be likely to result from the pyrolysis experiment. Primary attention would be focused on these compounds as being most representative of the data produced by the proposed experiment.

(2) Category II. The remaining compounds, obtained from various sources, form the second spectral library, which would be used primarily to assess the sensitivity of the results obtained from the Category I compounds to the choice of library.

After removing obvious errors and adding certain pertinent information, the formula of each compound was decoded from a character string (e.g., C10.H9.N.02) to a vector of elemental compositions (10, 9, 1, 2, etc.). All spectra were normalized in the conventional manner (the maximum intensity peak was assigned a value of 100.0).

In the merging process (Fig. 1), Category I compounds were obtained by eliminating the following spectra:

(1) All compounds containing halogens or deuterium.

(2) All non-hydrocarbons with molecular weight greater than 175.

(3) Compounds specifically suggested as unlikely by the experimental team.

(4) Redundant spectra of the same compound.

As a result of this elimination procedure, a Category I spectral library of approximately 1195 compounds has been obtained. Work is in progress to produce a non-redundant Category II library and to merge the MSDC data into the resultant libraries.

d. Data compression and interpretation of mass spectra. The interpretation of mass spectra is conventionally performed by comparing the fragmentation pattern of an unknown compound against a known spectral library. The intensities and positions (atomic mass) of each peak are the relevant information compared.

[1]Simmonds, P. G., "Organic Analysis of Soil Pyrolysis–GC/MS, a candidate for a Mars Lander," submitted to *Anal. Chem.*

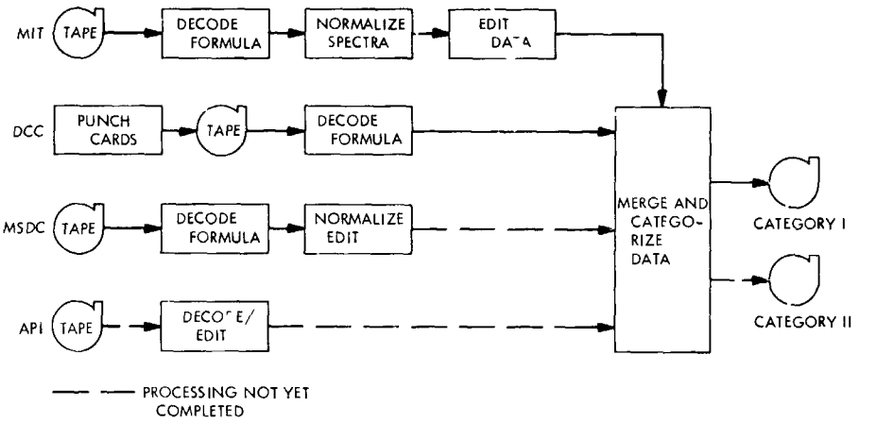

Fig. 1. Spectral library production

Because of the very large amount of data obtained in a short period of time from a GC/MS instrument, acquisition and spectral analysis procedures have been automated in many laboratories. Nevertheless, the automated interpretation of spectra is still in its infancy. Most of the existing schemes are too complex for on-board spectral identification.

A significant question yet to be answered is: Within the dictates of a proposed pyrolysis–GC/MS experiment and available flight instrumentation, what is the minimum number of bits required to provide the information necessary for compound identification? Several aspects of this question are under investigation using the spectral libraries described in *Paragraph c.*

Looking towards quantization and data compression, what is the distribution of peak heights in a mass spectrum? Figure 2 is a histogram showing the average percentage of peaks less than a given peak height versus peak height taken from the Category I library of 1195 compounds. It is important to note the nearly exponential behavior in height distribution which yields the result that about one-half of the total number of peaks in a

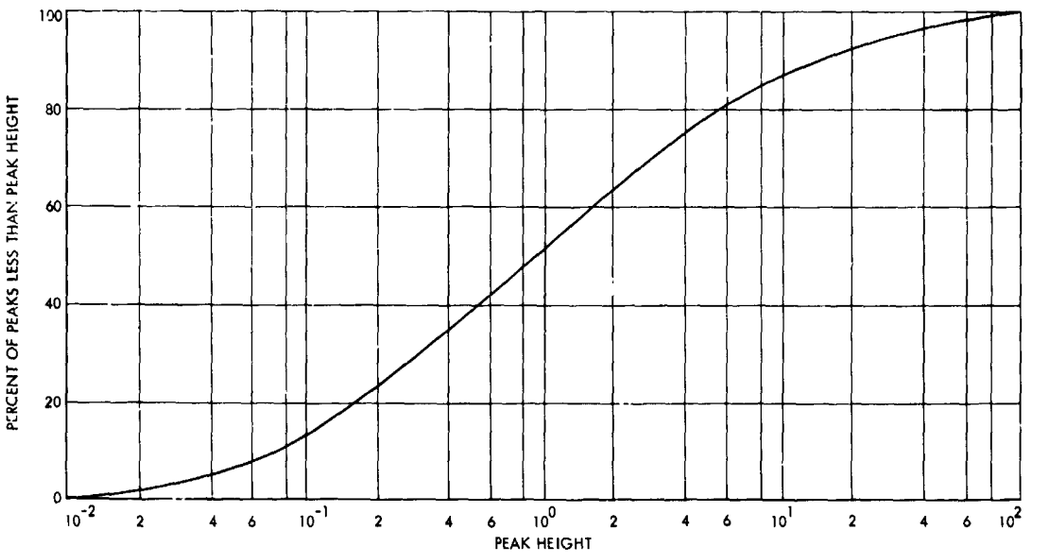

Fig. 2. Average percentage of peaks less than a given height vs peak height

mass spectrum lie below 1% of the maximum peak intensity. This factor will strongly influence the choice of a data compression scheme.

Various data-compression algorithms will be tested using the spectral library discussed in *Paragraph c.* A good illustration of the inter-relationships of instrument behavior, mass spectral characteristics, and data compression is provided in the following simple comparison. Assume that a mass spectrum, covering a range of M mass units, in which each peak is quantized to B levels is encoded using two different, information-preserving schemes as follows:

(1) The peak height for *every* mass unit is encoded, irrespective of the absence or presence of a peak, resulting in a constant total number of bits ($M*B$) required per spectrum.

(2) A pair of numbers is encoded, representing the position and height of each peak above a detectable ionization current set by instrument characteristics. In this case, a non-constant number of bits is required equal to $N*(B+\log_2 M)$, where N is the number of detectable peaks.

Scheme (2) will involve fewer bits if the number of detectable peaks, N is less than $M*B/(B+\log_2 M)$. The number N will depend on the dynamic range of the instrument and the amount of sample available for analysis.

The following parameterization illustrates these results. Assume a mass spectral range of 128 (7 bits), and assume that each peak is quantized to 3, 4, or 5 bits. Also assume that experimental conditions and instrument sensitivity make it possible to detect peaks only above 0.01, 0.1, 1, and 10% of the maximum intensity peak. For the Category I library of 1195 compounds, Table 1 gives the percentage of compounds for which scheme (2) requires fewer encoding bits than does scheme (1). It can be seen that the relative encoding efficiency of the two schemes depends quite critically on the detectable peak height.

Table 1. Relative efficiency of schemes (1) and (2)

Minimum detectable peak height,[a] %	Number of quantization bits		
	3	4	5
0.01	12	23	32
0.1	16	30	41
1.0	70	85	92
10.0	99.8	100	100

[a]base peak = 100

The above example illustrates the types of comparison that are planned using the spectral library. It should be obvious that these results have ramifications beyond the primary goal of data compression. As the example shows, there is an obvious relevance to instrument design.

In addition to the spectral data analysis and data compression programs, a set of programs has been developed for automatically identifying mass spectra. Although computer identification studies have been done in the past, the present work will consider the following three aspects of the problem, which have received little or no attention:

(1) A comparison will be made of the efficiencies of different identification schemes. Whereas many authors have proposed criteria for identification, little has been done in regard to comparing these schemes in terms of efficiency of identification, program storage, and timing requirements.

(2) The programs developed have the capability of simultaneously comparing spectra by any of a large number of criteria. The comparative ranking by "goodness of fit" is available as the search through the library proceeds. In this comparison, either components in the library or unknowns can be used.

(3) Virtually nothing has been published on the identification of data-compressed or noisy spectra. The identification programs have been structured in such a way as to facilitate this type of comparison. It is planned to compress the Category I library using various compression schemes and to investigate the resulting identification problems.

e. Additional investigation. Further studies will be concerned with the following:

(1) The completion of spectral library compilation by adding new compounds as obtained.

(2) The further investigation of relevant mass spectra data characteristics, particularly as related to compression/identification algorithms.

(3) The comparison of characteristics (efficiency, hardware implementation, storage, speed, etc.) of various compression/identification schemes.

(4) The use of actual flight instrument data, when available, to verify or modify the conclusions obtained from the spectral library.

References

1. Kaiser, R. W., and Sullivan, R. E., *Anal. Chem.*, Vol. 40, pp. 273R–302R, 1968.
2. *Advances in Mass Spectrometry, Volume IV.* Edited by E. Kendrich. Institute of Petroleum, London, 1968.
3. Crowford, L. R., and Morrison, D., *Anal. Chem.*, Vol. 40, p. 1464, 1968.

2. Peak-Height Distribution of Mass Spectra

The necessity for the efficient encoding of a large volume of mass spectral data was discussed in *Subsection 1.* The proposed method of solution proceeds through the following stages:

(1) The development of a library of actual mass spectral data for a wide class of organic compounds.

(2) The determination of the statistical properties of these spectra.

(3) The development of a model incorporating the derived statistical features.

(4) The use of this model to derive data compression algorithms.

A library of approximately 3400 organic compounds of molecular weights 16–536 has been accumulated on digital magnetic tape. The results discussed here were obtained from this library using an IBM 7094 computer for calculations. An additional 1500 compounds are expected to be added to the library shortly.

The distribution of peak heights is an important statistical characteristic for data compression purposes. In any digital encoding of peak height, for example, transitions between levels must be set. The knowledge of the peak-height distribution will aid in the optimum setting of these levels so as to assure maximum information content.

Mass spectral peak heights are conventionally normalized so that the maximum intensity peak (base peak) is assigned a value of 100. The data on peak heights in the library cover a dynamic range of 10^4, i.e., the minimum measurable peak height is 0.01% of the base peak.

The cumulative peak-height distributions for three groups of organic compounds are shown in Fig. 3. The characteristics of these groups are listed in Table 2. Group 1 consists of a heterogeneous collection of 3166 organic compounds. Group 2 is a special subset of the first group containing 1084 compounds selected as discussed in *Subsection 1.* These compounds were thought to be particularly relevant to a proposed pyrolysis experiment. Group 3 consists of 512 compounds, all with molecular weights less than 101.

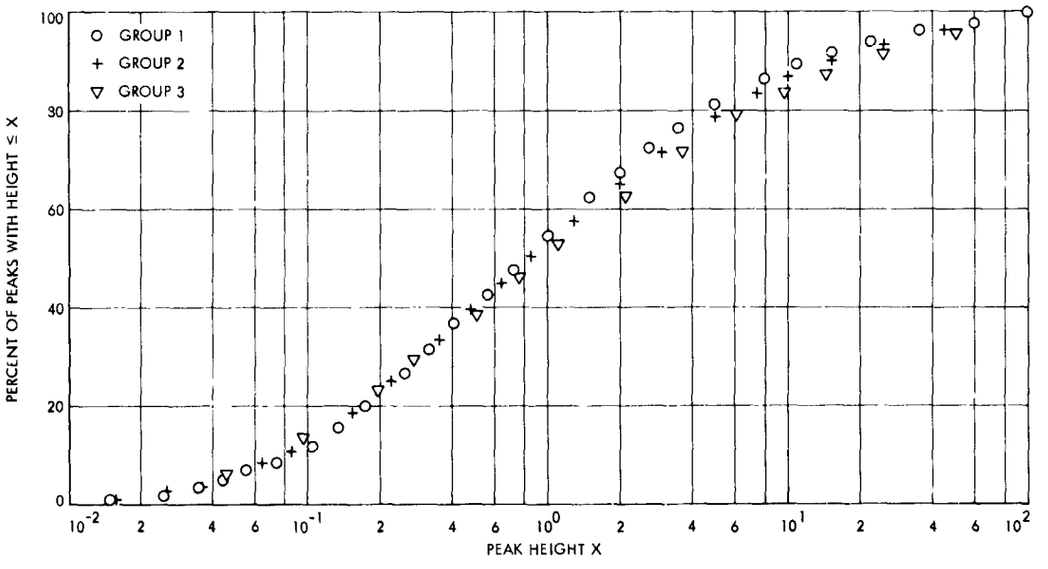

Fig. 3. Cumulative peak-height distributions for three groups of organic compounds

Table 2. Group characteristics

Group	Number of compounds	Average molecular weight	Average peaks/spectrum
1	3166	158	84
2	1084	132	72
3	512	79	46

Several characteristics are evident from Fig. 3. Firstly, the three collections of compounds have approximately the same distribution of peak heights, even though each group contains widely different average numbers of peaks per spectrum. Other subgroups of this set of compounds exhibit this same characteristic. Thus, a particularly useful conclusion can be drawn: The distribution of peak heights in a collection of mass spectra appears to be approximately independent of the compounds comprising the assemblage. This is particularly important for the present study because the peak-height distribution should be insensitive to the choice of library considered.

It is also interesting to note that the mean peak height for a typical mass spectrum is only 1% of the base peak. The distribution of peak heights is highly non-linear, with a disproportionate number of smaller peaks present.

The cumulative peak-height distributions shown in Fig. 3 are replotted on a log-probability grid in Fig. 4. On this grid, a normally distributed variable plots as a straight line. It appears that the logarithm of the peak height is normally distributed, at least for peak heights greater than about 0.1% of the base peak. Since the raw spectral data were derived from several experimental sources and were not compared with published data, it is not unlikely that the records of peak heights in the library, particularly those below 0.1% of the base peak, could be in error.

Can these distributions be explained by a theoretical model? Unfortunately, the presently accepted theory of mass spectral formation (Ref. 1) does not permit such predictions, except for the very simplest molecules.

A model of mass spectral formation is proposed here consisting of a series of cascading reactions in which a parent ion disintegrates into m daughter products, each of which in turn disintegrates further into m daughters. If one assumes that all reactions are described by first-order kinetics, and that all rate constants are equal, the peak-height distribution for each spectrum is described by a slightly modified form of the Poisson distribution.

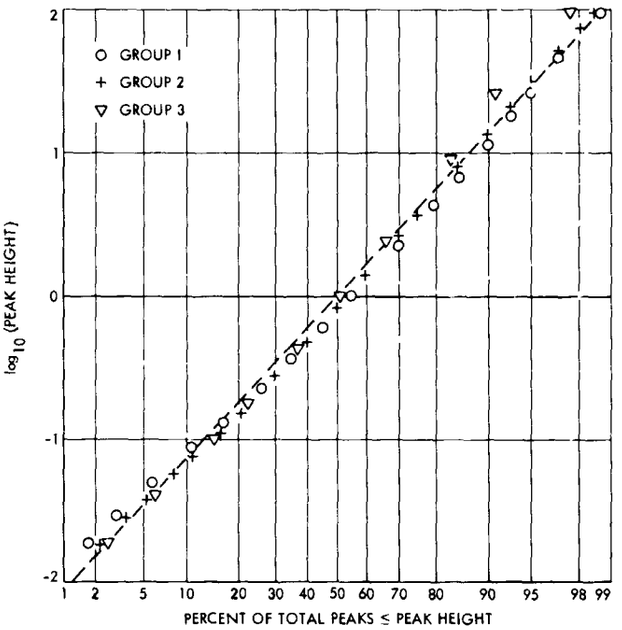

Fig. 4. Cumulative peak-height distributions log-probability plot

Preliminary calculations show that this model qualitatively predicts the distribution of Fig. 4. However, further refinement of the model and a better determination of model parameters are required before definite (quantitative) conclusions can be drawn.

Reference

1 Rosenstock, H. M., *Advances in Mass Spectrometry, Volume IV*. Edited by E Kendrich. Institute of Petroleum, London, 1968.

3. Experimental Study of Species Enrichment in a Supersonic Jet Separator

a. Introduction. The phenomenon of species separation in the stagnated supersonic flow of a binary gas mixture is currently under investigation as one method of obtaining sample enrichment in the effluent of a gas chromatograph column. Enrichment of the sample gas (typically diluted to 1000 parts/10^6 in a carrier gas) is required in order to permit real-time analysis by a mass spectrometer.

A number of gas chromatograph/mass spectrometer (GC/MS) instruments are in existence, several of which utilize a supersonic jet separator designed by R. Ryhage

(Ref. 1). A laboratory instrument in use at JPL is described in SPS 37-54, Vol. III, pp. 150–155.

In considering a separator for a flight instrument, however, size, weight, and power limitations place a great demand on separator efficiency. Since the optimum design for a supersonic jet separator is dependent on an understanding of the separation mechanism, a single-stage separator is being investigated. From earlier experimental data, it is reasonable to expect that a multiple-stage separator will be capable of achieving a sufficiently high amount of enrichment to be a candidate separator for the GC/MS instrument.

Two other types of separators are under consideration: (1) the Llewellyn separator, which consists of a pair of silicone-rubber diaphragms through which organic compounds diffuse leaving the carrier gas behind to be pumped away, and (2) the palladium separator, which, when heated, is highly permeable to the hydrogen carrier gas, thereby enriching the remaining sample gas.

The implications of several experimental studies of species separation in supersonic jets are important not only to the design of a separator per se, but also to the use of gas sampling systems in general. For example, the flow regime encountered by a supersonic planetary entry probe is similar to that occurring in a separator; hence, the gas mixtures observed in atmospheric analysis experiments may not be representative of the atmosphere through which the probe is passing.

This article summarizes much of the previous work on the problem of separation effects, describes the experimental work in progress at JPL, and presents a few preliminary results.

b. The separation mechanism. The generic configuration of a single-stage supersonic jet separator is shown in Fig. 5. A mixture of sample and carrier gases is introduced into the stagnation chamber (A). Under the influence of a pressure differential, the gas flows through a sonic orifice (B) and passes into the low-pressure chamber (C) forming an under-expanded supersonic jet. A sampling probe (D) for removing the enriched (higher sample concentration) gas is inserted into the jet. The remaining carrier gas and a fraction of the sample gas is removed from the separator through the high-speed exhaust line (E).

The separation phenomenon was encountered by several experimenters in the field of molecular beam research. It has been theorized by E. W. Becker (Ref. 2) that the separation effect could be explained by thermal diffusion and baro-diffusion in a freely-expanding jet. It is suggested by S. A. Stern, P. C. Waterman, and R. F. Sinclair (Ref. 3) that the separation effect was caused by the behavior of stream and thermal velocities of gases of differing molecular weights in near-free molecular flow. In 1963, V. H. Reis and J. B. Fenn (Ref. 4) conducted experimental investigations that suggested the prime consideration was the interaction between the sampling probe and the gas jet. These investigations, combined with the theoretical investigations of diffusive separation of gas species in a free jet performed by F. S. Sherman (Ref. 5), are convincing arguments that the reported separation effects are primarily probe-induced.

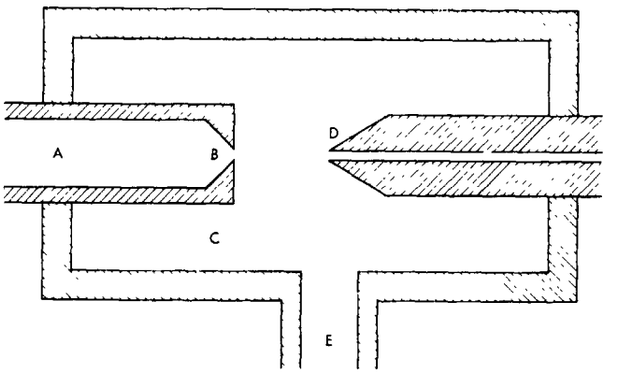

Fig. 5. Schematic diagram of a typical separator

The axi-symmetric free jet. The nature of the flow originating from a sonic orifice with a greater than critical pressure ratio has been investigated by aerodynamicists for a number of years. The shockwave pattern is shown in Fig. 6.

The Mach number has been observed to increase monotonically with distance downstream of the nozzle until the normal shock wave is reached. A method-of-characteristics solution for the axial Mach number distribution was accomplished by P. L. Owen and C. K. Thornhill (Ref. 6), and their results have been experimentally verified. In Ref. 7, H. Ashkenas and F. Sherman give the relation

$$M = A\left(\frac{x - x_0}{D}\right)^{\gamma-1} - \frac{1}{2}\left(\frac{\gamma+1}{\gamma-1}\right) \Big/ A\left(\frac{x - x_0}{D}\right)^{\gamma-1} \quad (1)$$

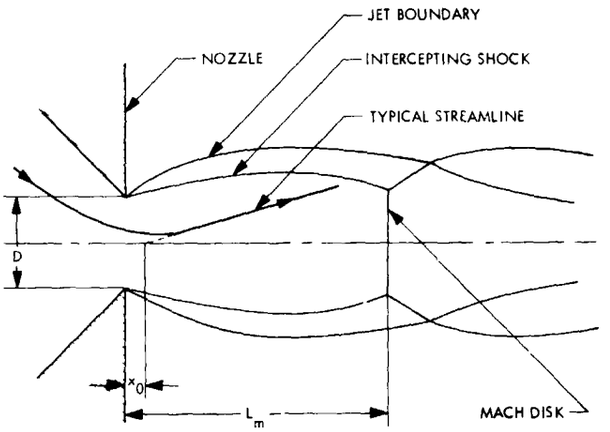

Fig. 6. Jet structure behind a sonic orifice or nozzle

where x is the downstream distance from the nozzle exit, D is the nozzle diameter, and γ is the specific heat ratio. The constants A and x_0/D are given in Table 3. At a distance L_m from the nozzle exit plane, a normal shock (Mach disk) occurs given by the relation

$$\frac{L_m}{D} = 0.67 \left[\frac{p_{01}}{p}\right]^{1/2} \tag{2}$$

where p_{01} is the total pressure in the nozzle and p is the background pressure. It is thought that the gas expansion is independent of the background pressure until the Mach disk is reached.

The region between the nozzle and the first Mach disk is the region of interest. The flow is termed "self-similar" with stream lines radiating from an apparent point source at distance x_0 from the nozzle exit. Correspondingly, the density decreases along each stream line in inverse proportion to the square of the distance from the source. If the background pressure is very low, the gas may undergo a transition from continuum to free molecular flow. In the molecular flow region, the translational energy of the gas and the Mach number are constant. The terminal Mach number is given by the empirical relation

$$M_T = 1.17\, Kn_1^{(1-\gamma)/\gamma} \tag{3}$$

Table 3. Constants for jet flow properties

γ	X_0/D	A
1.67	0.075	3.26
1.40	0.40	3.65

where Kn_0, the nozzle Knudsen number, is the ratio of the viscosity-based mean free path in the nozzle stagnation chamber to the nozzle diameter.

Interaction of a probe with the jet. A shock wave pattern develops around a probe immersed in a supersonic jet. Although early experimenters ignored or attempted to minimize shock effects, sufficient data has been obtained to indicate that the interaction of the supersonic stream with curved shock waves and the flow in the intermediate post-shock region are the major sources of the separation effect. Not until recently have the probe geometry and sampling line flow rate been considered.

The bow shock wave, which forms around the upstream end of the probe, can be either attached to the probe, as in the case of cones of small semi-vertex angle, or detached, as in the case of cones of larger semi-vertex angle and blunt nosed objects. The detachment distance is determined by the probe geometry and the free stream Mach number. When gas is withdrawn through an opening in a probe, a bow shock wave can be swallowed, i.e., attached to the edges of the entry orifice. Experiments have indicated that separation effects occur only when the bow shock wave is detached.

The shock-wave problem. Having localized the source of the separation effect to the bow shock wave and post-shock region, the problem is far from solved. The problem is the structure of a curved shock wave in a binary gas mixture and the nature of the flow of the different gas species near the shock. The problem is particularly difficult for several reasons. First of all, the convenient assumption that the separate gas species maintain thermal equilibrium, which requires frequent intermolecular collisions, is not valid in many regions of the low-density jet. Secondly, the strength and spatial extent of a shock wave in the rarified flow of a binary mixture are not clearly defined. Thirdly, experimental determinations of the magnitude of the separation effect are affected by diffusive recombination of the gases in the shock and post-shock region.

In one of the more extensive experimental investigations, J. H. Chang (Ref. 8) has attempted to correlate the measurements of enrichment with some of the aerodynamic dimensionless groups. Such correlations summarize the effects of many variables and focus attention on the pertinent physical conditions contributing to the observed effect. The dimensionless group $(Kn/M)_\infty$, where Kn_∞ is a Knudsen number determined by the ratio of the

free-stream mean free path to the probe outside diameter, and M_∞ is the free-stream Mach number at the probe location, appears to be a useful parameter. The Mach number indicates some of the important properties of the jet and the Knudsen number relates the state of rarefaction of the gas to the characteristic size of the sampling probe. Chang observed that for a particular initial gas mixture, the greater the ratio $(Kn/M)_\infty$, the greater the observed separations. This parameter does not, however, correlate results obtained with one binary gas mixture to those obtained with another. Thus, the effects of differing initial mole fractions, as well as differing gas species, are not included in such a correlation. The molecular weights and specific heat ratios of the individual gas species must be incorporated into an empirical representation of the separation effect, and it appears that more experimental work must be done before even a satisfactory empirical relation can be found.

c. The experimental apparatus. The experiment presently being conducted differs in three ways from most of the previous experimental measurements of separation phenomena in supersonic jets:

(1) As a result of the desire to investigate much smaller flow rates, the physical size of the separator system is considerably smaller than those investigated by others.

(2) Provisions have been made to meter inlet and outlet flow rates in order to determine the amount of sample lost in the separation process, which is an important aspect of the efficiency of the separator.

(3) The flow regime is being viewed by means of a Schlieren optical system in order to visualize the major features of the flow field.

Separator assembly. The test model single-stage separator is shown in Fig. 7. The 0.25-in. inlet line passes through a modified Swagelok union and is terminated by a conical plug having a 0.002-in. diam orifice. The sampling probe passes through an identical fitting and is

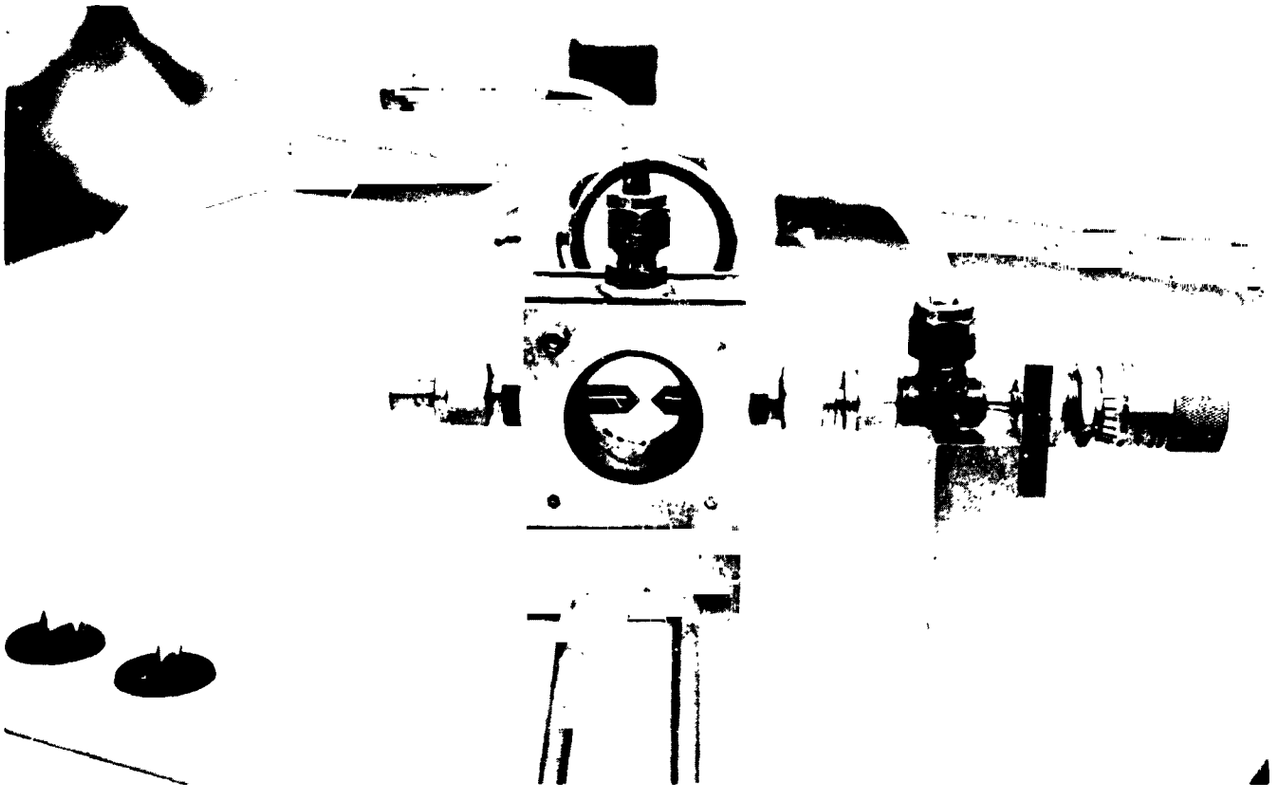

Fig. 7. Test model separator assembly

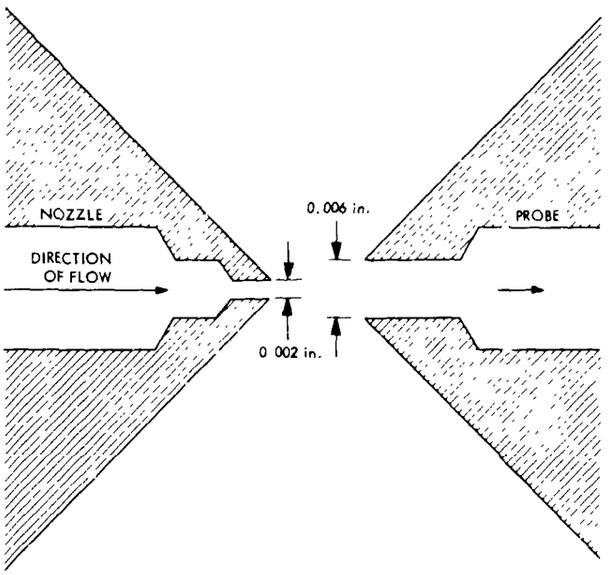

Fig. 8. Nozzle and probe configuration

terminated by a 45 deg half-angle cone with a 0.006-in. orifice (Fig. 8). A sliding seal is made between the Teflon Swagelok ferrules and the probe afterbody, which is coated with a thin layer of Apiezon vacuum grease. The probe axial position relative to the nozzle orifice can be set to ±0.0001 in. by means of a micrometer screw drive. The separator exhaust line exits through the top of the separator.

The side walls of the separator are 0.25-in. thick glass optical flats resting upon 1.25-in. diam O-rings, and are held in place by pressure plates. The glass windows allow the nozzle and probe alignment to be checked and permit Schlieren photographs to be taken.

Flow system. The arrangement of the apparatus is shown schematically in Fig. 9. Pre-mixed gas samples have been analyzed by mass spectrometry to determine the sample concentration. The gas mixture presently being used is 10.02-mol % nitrogen, the balance being hydrogen. The inlet flow rate and pressure are measured prior to its introduction into the separator.

A pressure gage located in the exhaust line indicates the background pressure in the separator. A throttling valve in the line allows the background pressure to be controlled. For the inlet flow rates encountered in the experiment, a background pressure as low as 3.0 torr can be maintained by a Welch Duo-Seal mechanical pump with a speed of 7 l/s.

The composition of the sampled gas is determined by comparison of the pressure readings of an NRC 820 Alphatron and a 0–100-torr Wallace and Tiernan diaphragm-type gage. The response of the Alphatron strongly depends on the gas composition. After calibration with gas mixtures, the ratio of the Alphatron pressure to the measured total pressure indicates the mole fraction of the sampled gas to the nearest mole percent.

A throttling valve located downstream of the gas analysis chamber allows the sample flow rate to be varied and acts as a restrictor prior to the vacuum system. The sample flow rate is determined by the pressure drop across a 0.125-in. orifice. Thermocouple and ionization gages are located on both sides of the orifice in order to measure the pressures. The system is pumped by a 60-l/s oil-diffusion pump with a mechanical fore-pump.

The optical system. The image contrast in a Schlieren system is determined primarily by the density gradients in the flow field; thus even though the gas density is low, the gradients are sufficiently strong to be observed.

The optical arrangement of the Schlieren system is shown in Fig. 10. Illumination is provided by a high-intensity incandescent lamp whose image is focused on an adjustable source slit to provide a rectangular source image. The source slit is at the focal point of lens 1, thereby producing a parallel illuminating beam that passes through the optical flats forming the walls of the separator. The orifice and probe are located in the focal plane of lens 2 and, hence, their shadow image is formed on the film plane of the camera, which is focused at infinity. A knife-edge, located at the focal point of lens 2, is adjusted to intersect approximately half of the image of the source slit. Those rays that have been refracted in passing through density gradients will either be blocked by the knife edge, causing a relatively dark region in the image, or will pass the knife edge unobstructed, forming a relatively light region in the image depending on the direction of the density gradient.

The camera is a Kodak Retina Reflex with a 200-mm telephoto lens. Since the focal length of lens 2 is also approximately 200 mm, the image on the film plane is in approximately a one-to-one ratio with the separator test section.

d. Preliminary results. Some preliminary measurements of sample enrichment have been made for the

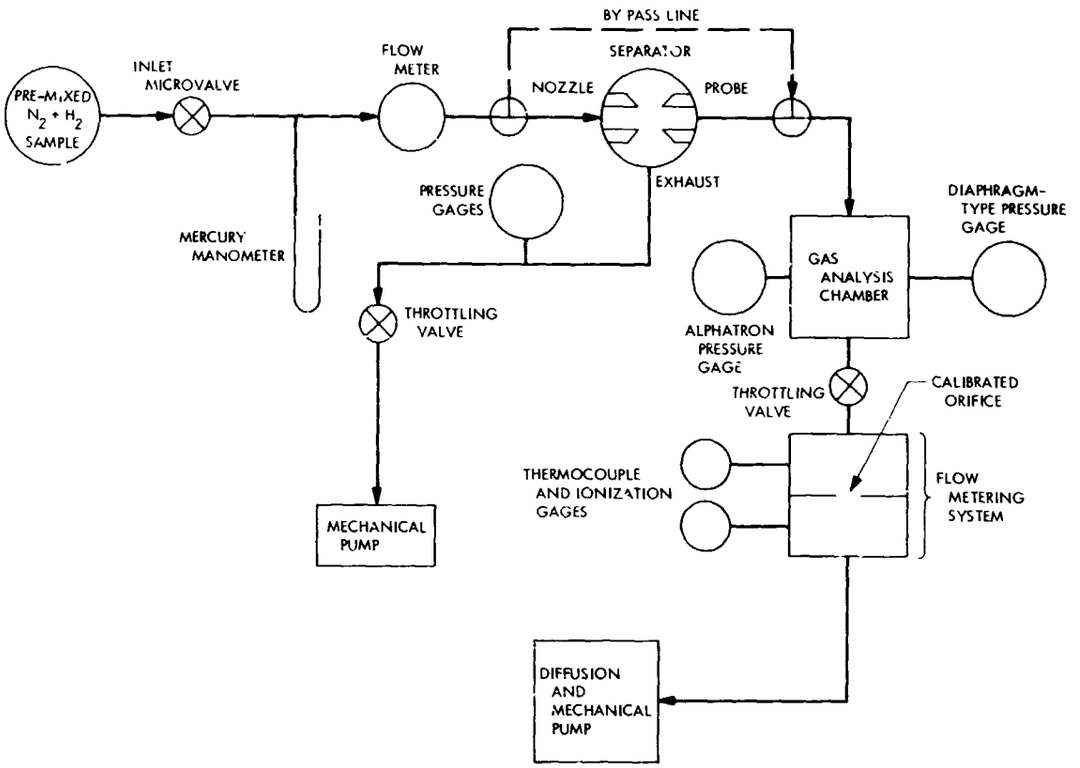

Fig. 9. Separator flow test apparatus

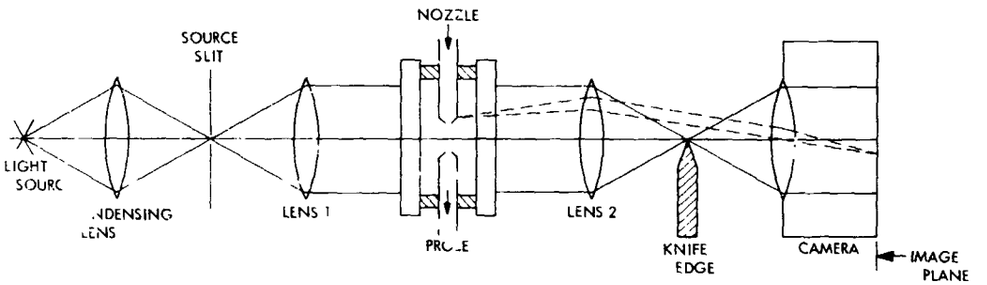

Fig. 10. Schlieren viewing system

nozzle and probe geometry shown in Fig. 8. The conditions under which the measurements were made are listed in Table 4

It was found that the measurement of impact pressure, as indicated by a Wallace and Tiernan gage in the gas-analysis chamber, was unaffected by the small extraction line flow rate. Hence, the impact pressures shown in Fig. 11 were obtained with a finite flow rate through the gas-analysis chamber. The first minimum in the

Table 4. Measurement conditions

Supply pressure	760 torr
Inlet flow rate	55 standard cm^3/min
Inlet gas composition	10.02 mol % N_2; balance H_2
Background pressure	5.0, 10.0, and 20.0 torr
Flow rate through sampling probe	0.17 standard cm^3/min
Temperature at inlet	25°C
Nozzle-to-probe distance	Varied from 0.005 to 0.030 in.

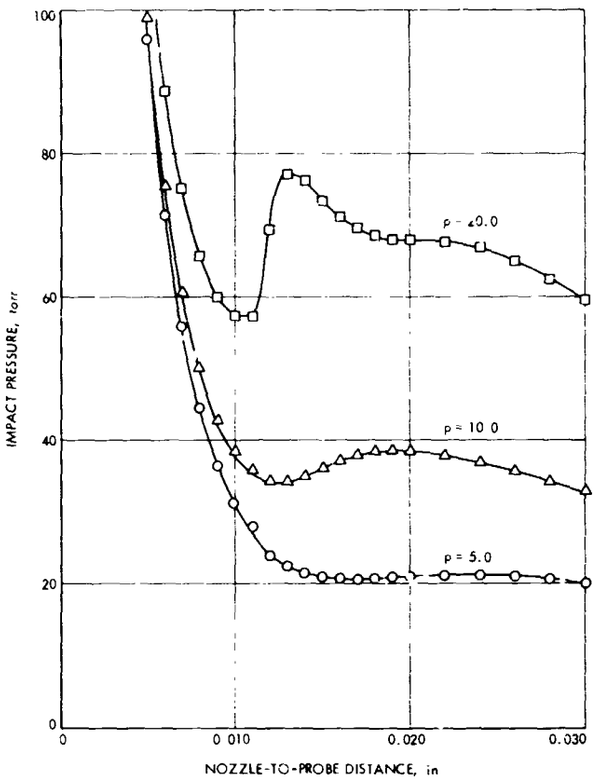

Fig. 11. Axial impact pressure profiles

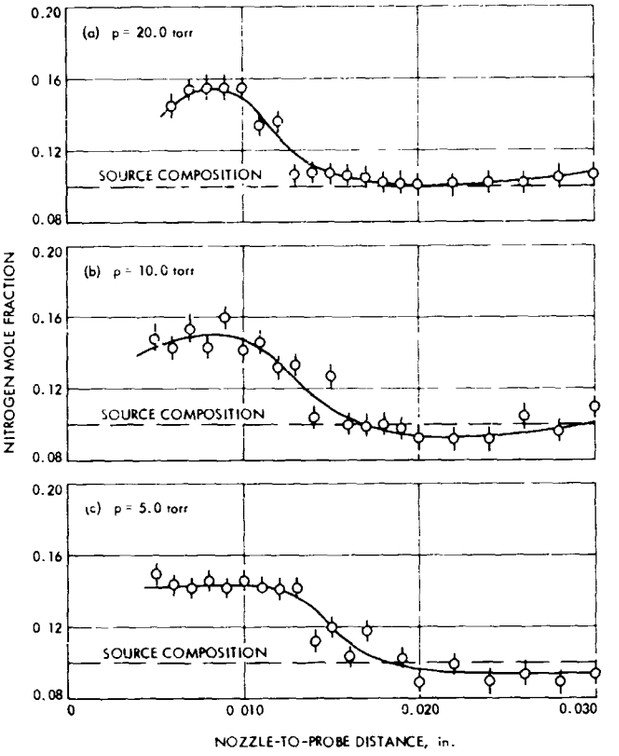

Fig. 12. Axial sample composition profiles

impact pressure curve indicates the location of the Mach disk. The minimum is well defined for a background pressure of 20.0 and 10.0 torr, however, at 5.0 torr, its location is not as easily discerned. Assuming the validity of Eq. (2), the Mach disk locations imply an effective nozzle orifice diameter of 0.0021 in. The effective orifice diameter is, in general, smaller than the geometrical diameter because of the development of viscous boundary layers within the nozzle; however, the effective diameter determines the scale of the flow regime, and is the value referred to in Eqs. (1), (2), and (3).

Figure 12 shows the measured sample gas composition obtained in axial traverses at three different background pressures. The maximum sample concentration observed in these measurements was 16% (an enrichment factor of 1.6). The most important observation is that the decrease in sample concentration occurs as the Mach disk location is reached. This correlation, noted by other experimenters, is strong evidence that separation effects occur in the bow shock wave preceding the sampling probe. In the two lower pressure curves, there is an indication of sample depletion or "negative separation," an effect also observed by others. The data at hand is not sufficiently precise to place much importance on these regions of the curves.

Schlieren photographs, taken under the conditions described earlier, show gas density gradients in the flow field; however, the variations in intensity in the photographs are small. A technique in which the negatives are scanned by a recording photodensitometer is being investigated. The record of such a scan may be numerically integrated to give a density profile of the flow field. This type of data would provide information unavailable from flow and pressure measurement, viz., the location of the bow shock wave relative to the probe.

e. Implications of the results for continuing investigation. In view of the limited amount of data accumulated so far, few conclusions can be drawn. However, a few comments about the results can be made, and the direction that the investigation will take in the future can be discussed.

The enrichment figures described above are smaller than those measured in other experiments [Chang (Ref. 8)

observed enrichment factors of 5 for the same initial gas mixture]. The probe configuration is a subject for closer scrutiny. The conical shape (originally chosen because it is similar in shape to that used in the Ryhage design) does not have a characteristic outside diameter because the probe is many times larger than the entire flow field. The problem of Reynolds number corrections to probe impact-pressure measurements is intractable. Furthermore, a realistic estimate of the probe Knudsen number cannot be made. Thus, correlations with the dimensionless group $(Kn/m)_\infty$ are impossible. To correct these problems, a probe terminating in a 0.012-in. OD capillary tube with a length-to-diameter ratio of 8 has been constructed (Fig. 7).

In addition to the probe configuration, future work will be concerned with the effect of extraction line flow rate on sample loss. Measurements of enrichment for heavier sample gases than nitrogen are needed to evaluate the effectiveness of the supersonic jet separator in separating organic molecules from hydrogen carrier gas. Finally, the investigation of a multiple-stage separator, the design of which should be facilitated by the experimental study, can be accomplished.

References

1. Ryhage, R., *Ark. Kem.*, Vol. 26, p. 304, 1967.

2. Becker, E. W., *Separation of Isotopes*, p. 360, George Newnes, Ltd., London, 1961.

3. Stern, S. A., Waterman, P. C., and Sinclair, R. F., *J. Chem. Phys.*, Vol. 33, p. 805, 1960.

4. Reis, V. H., and Fenn, J. B., *J. Chem. Phys.*, Vol. 39, p. 3240, 1963.

5. Sherman, F. S., *Phys. Fluids*, Vol. 8, p. 773, 1965.

6. Owen, P. L., and Thornhill, C. K., Aeronautical Research Council Reports and Memoranda 2616, Great Britain, 1948.

7. Ashkenas, H., and Sherman, F., *Rarefied Gas Dynamics, Supplement 3, Volume II*, p. 84. Edited by J. H. deLeeuw. Academic Press, New York, 1966.

8. Chang, J. H., *Species Separation of Gas Mixtures in Supersonic Flow*, Princeton University, 1967.

C. Guidance and Control

1. Orbiter Power Subsystem

a. Introduction. The *Viking* orbiter baseline power subsystem is essentially a major modification of the *Mariner* Mars 1971 power subsystem. The modifications are necessitated by the following guidelines and constraints:

(1) An orbit insertion mode with approximately 167 min of off-sun-line operation and a burn time three times as long as *Mariner* Mars 1971 is the worst case energy demand period.

(2) One-hundred days of Mars orbital operation with partial sun occultation during approximately 50 days.

(3) The requirement for providing 5–182 W of *Viking* lander capsule power during the transit and early orbital period.

(4) A revised science payload.

(5) A greater sun–Mars distance than *Mariner* Mars 1971 resulting in a 28% decrease in available solar panel power at the time of arrival (March 20, 1974).

The above factors have necessitated a revision in the power subsystem philosophy established on previous *Mariner* spacecraft. The battery selected for this mission must be capable of providing approximately 70–75 flight cycles after the 6–7 mo transit period. In addition, the battery also will be used to supplement the solar panels during the *Viking* lander capsule checkout period. The solar panels have been sized for the mode of operation requiring battery charging towards the end of the 90-day orbital cruise period.

b. Power requirements. A mission power profile depicting the total power requirements as compared to an operational mode of events is shown in Table 5. Total raw power required during the period of orbit-insertion maneuver to a post-sun-occultation mode will vary from 330 to 518 W. Of significance are the battery charging requirements of 125 W, the traveling-wave tube (TWT) subsystem continuous requirement of 96 W, and the approximate 3-h *Viking* lander capsule checkout requirement of 182 W. During the orbit-insertion mode, the orbiter is off the sun line for 167 min, and the total battery energy consumed is 1195 W-h. Approximately 260 W-h of this total are primarily due to the additional 30 min of orbit-insertion burn time that will occur wth single motor operaton. Figure 13 depicts this period, which is the basis for the sizing of the battery.

c. Solar panel. The primary power source selected for this mission is based on *Mariner* Mars 1971 solar cell technology. However, when projecting this technology

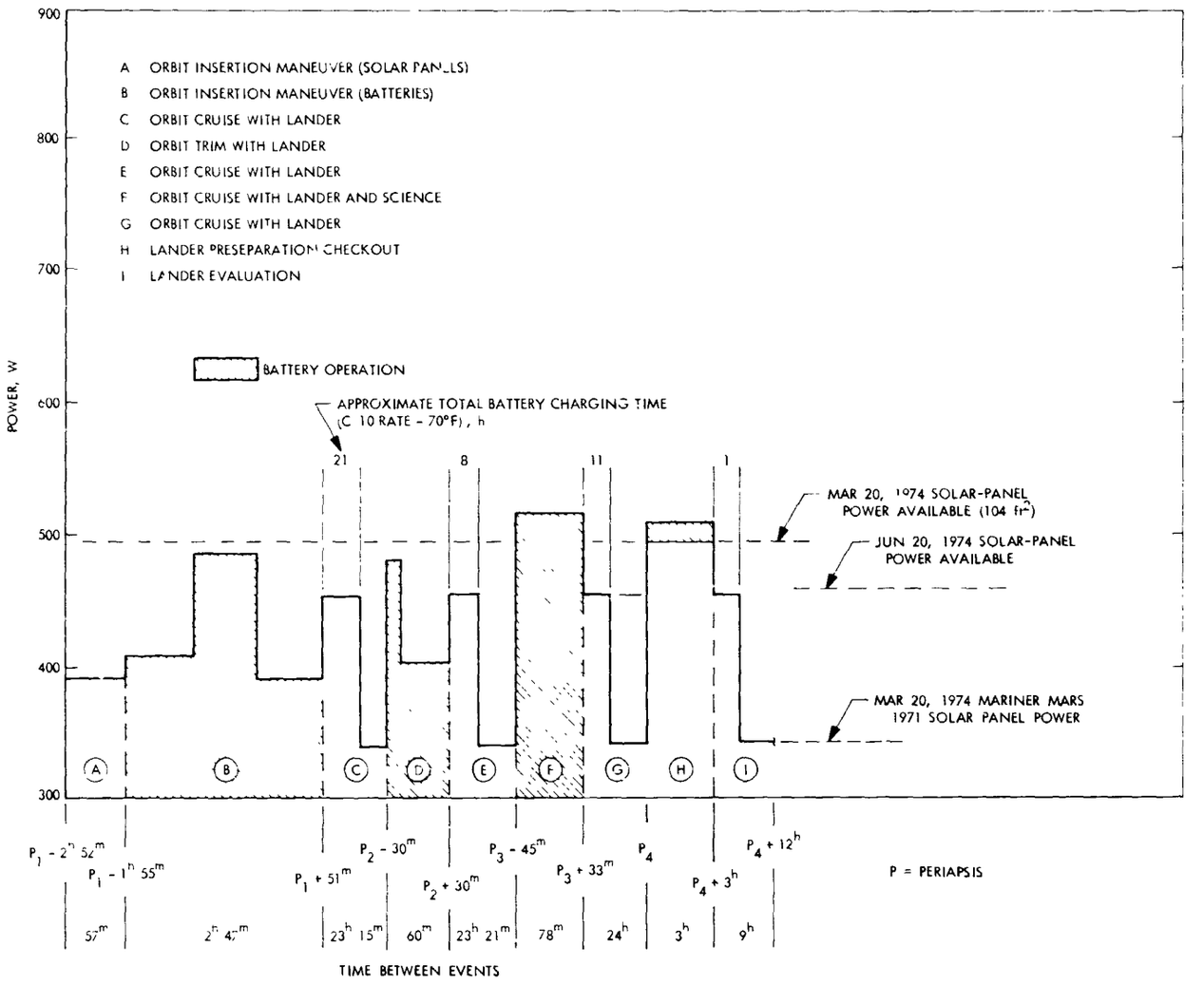

Fig. 13. Preliminary power profile

to a March 20, 1974 arrival date, a significant loss in performance occurs due primarily to the increased distance of the sun with respect to Mars. Figure 14 compares the sun–Mars distance for the *Mariner* Mars 1971 arrival date with that of the *Viking* arrival date.

At the time of arrival, Mars is approximately 1.62 AU from the sun, equivalent to 53.2 mW/cm². Solar cell performance is estimated at 5.80 W/ft² (−10°C). However, a conservative estimate of 10% degradation due to solar flare activity and an 8% reduction due to uncertainties in predicting the nominal power due to measurement limitations reduced the specific power to 4.75 W/ft² (−10°C) at arrival. The specific power is further reduced to 4.45 W/ft² (−16°C) 90 days after arrival. An additional 2% radiation loss is assumed for this time period. Based on a preliminary load analysis for this period, 461 W of raw power are required. On this basis, the total active solar panel area required would be approximately 104 ft². Total power at the time of arrival is 494 W and degrades to 464 W after 90 days. (At arrival, the *Mariner* Mars 1971 solar panels, consisting of 74.7 ft² of active area, would produce approximately 354 W.) The present baseline solar panel configuration (Fig. 15) consists of four rectangular panels each with 26 ft² of active solar panel area.

Table 5. Preliminary power profile

Operational mode	Power required, W	Source	Operational mode	Power required, W	Source
Launch	326	Battery	Orbit cruise with lander capsule	463	Solar panel
Sun acquisition	338	Battery	Lander capsule preseparation checkout	507	Solar panel/ battery
Cruise I—battery charge on (gyros off)	434	Solar panel			
Cruise II—battery charge off	296	Solar panel	Lander capsule evaluation and assessment	473	Solar panel
Cruise III—lander capsule checkout	366	Solar panel	Gyro warm up (bioshield capsule jettison maneuver)	390	Solar panel
Maneuver	469,[a] 357[b]	Battery			
Cruise I—battery charge on	434	Solar panel	Bioshield capsule jettison maneuver	390	Solar panel
Cruise II—battery charge off	334	Solar panel	Bioshield capsule jettison maneuver	401	Battery
Encounter	445	Solar panel	Lander capsule separation maneuver	373	Solar panel
Gyro warm up on	378	Solar panel	Lander capsule separation	387	Battery
Orbit-insertion maneuver	391	Solar panel	Lander capsule separation maneuver unwind	387	Solar panel
Orbit-insertion maneuver	403	Battery	Adapter bioshield capsule jettison maneuver	461	Solar panel
Orbit-insertion maneuver burn	518	Battery	Entry relay	333	Solar panel
Orbit-insertion maneuver and unwind	389	Battery	Orbital science on	430	Solar panel
Orbit cruise v lander capsule	463	Solar panel	Orbital science playback	330	Solar panel
Orbit trim with lander capsule	518,[c] 406[d]	Battery	Orbital cruise (sun occultation)	360	Battery
Orbit cruise with lander capsule	463	Solar panel	Orbital cruise with battery charge	461	Solar panel
Orbit cruise with lander capsule and science	515	Battery			

[a]15 s on. [b]1 h on. [c]1 min on. [d]59 min on.

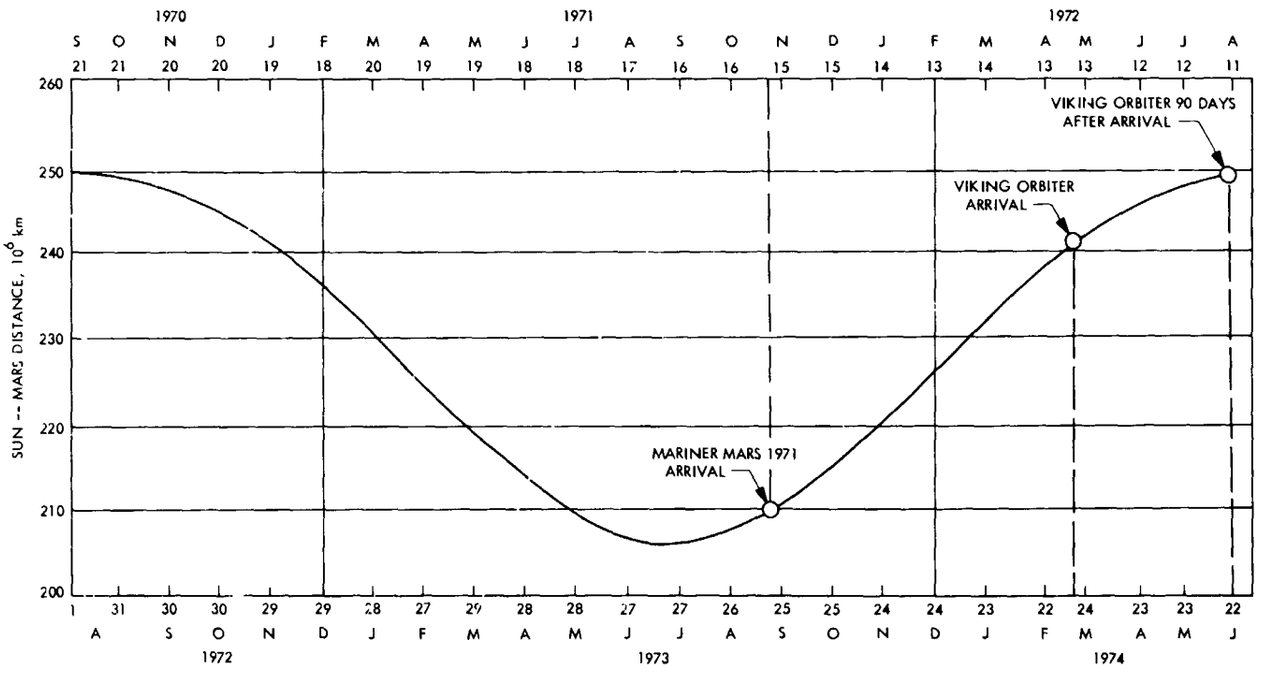

Fig. 14. Comparison of the sun–Mars distance for *Viking* orbiter and *Mariner* Mars 1971 arrival dates

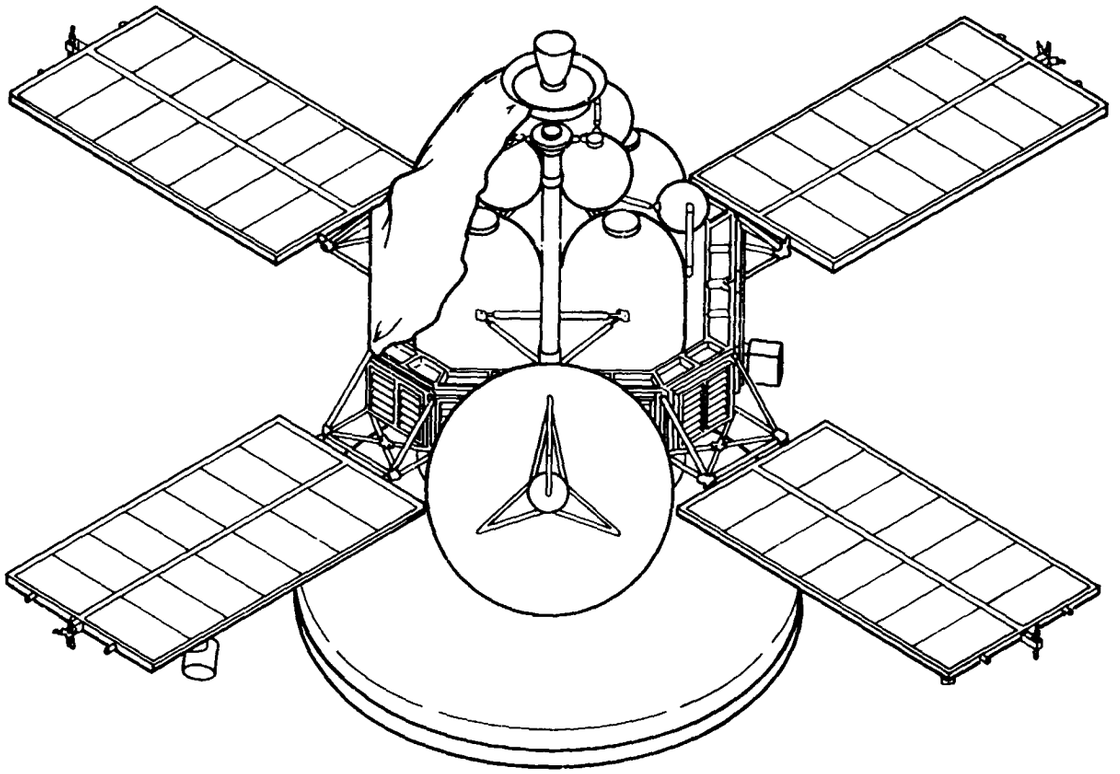

Fig. 15. Baseline *Viking* orbiter solar panel configuration

d. Battery. The desire to achieve a total of approximately 70–75 flight discharge/charge cycles including approximately 50 sun occultation periods has necessitated the use of hermetically sealed nickel–cadmium batteries, because of their cyclic capability. Total energy consumed during a worst-case period of operation (167 min off the sun line for the orbit-insertion mode of operation) is 1195 W-h. Total battery energy is estimated to be 1705 W-h based on a 70% depth of discharge. During the maximum 2-h sun occultation periods, a total of 720 W-h are consumed, representing a depth of discharge of approximately 42%. Two 30-A-h batteries that are discharged in parallel and charged sequentially have been selected in order to reduce solar panel area by approximately 28 ft². Each 30-A-h battery consists of 24 cells with a battery potential ranging from 32.5 to 26.5 Vdc.

Battery chargers are provided for replacing energy consumed during normal battery operation. In addition, periodic charging is performed during the transit period to replace energy lost due to the charge retention characteristics of nickel–cadmium batteries. Trickle charging during this period is also an option. The charging of the 30-A-h batteries in this configuration is accomplished with constant current at the C/10 rate (3 A) and constant potential, current limited. Sufficient time is available throughout the mission for the accomplishment of this objective.

e. Power conditioning. The *Viking* orbiter baseline power conditioning (Fig. 16) utilizes the *Mariner* Mars 1971 technology with the addition of some modifications to the booster regulator in order to accommodate increased power requirements. The system provides regulated dc power, derived from a dc–dc converter booster regulator, to individual inverters which provide the following:

(1) 2.4-kHz, single-phase squarewave power.

(2) 400-Hz, three-phase quasi-squarewave power.

(3) 400-Hz, single-phase squarewave power.

A separate dc–dc converter provides regulated 30-Vdc power from the unregulated raw bus to power the propulsion valves and gimbals.

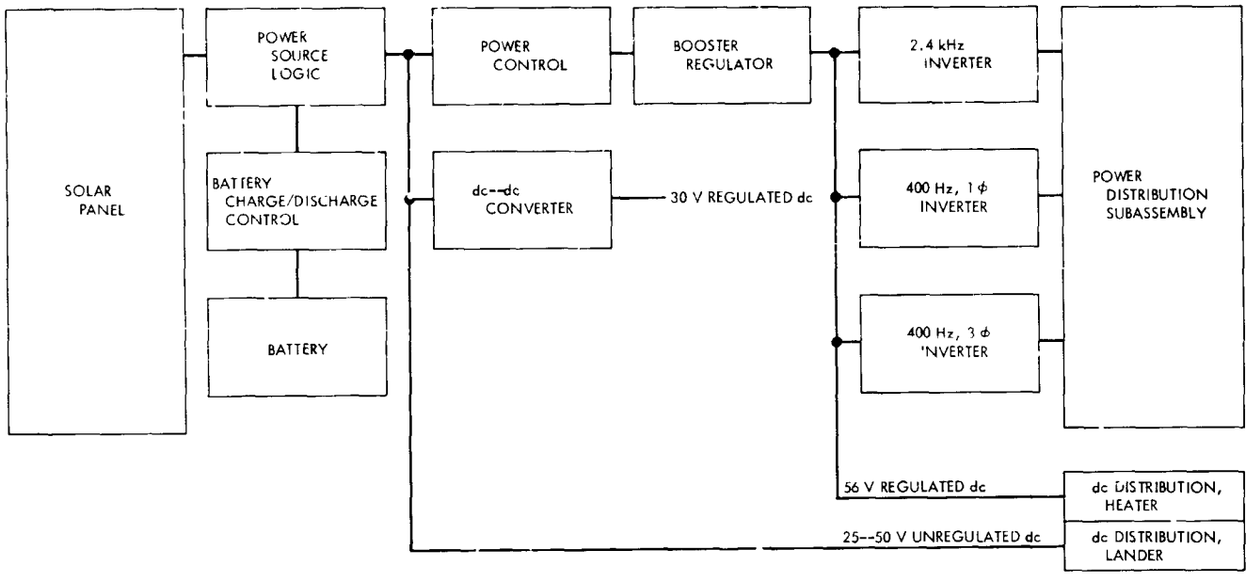

Fig. 16. Preliminary power conditioning subsystem

Booster regulator. The main booster regulator is designed to provide regulated power to all the *Viking* orbiter loads with the exception of the TWT subsystem, the propulsion valves and gimbals, and the *Viking* lander capsule. The output voltage is a regulated 56 Vdc at a tolerance of ±1%. Due to the increased *Viking* orbiter power requirements, the *Mariner* Mars 1971 main booster regulator must be upgraded to approximately 305 W. An identical standby booster regulator serves as a backup to the main booster regulator and will provide power to the *Viking* orbiter loads in case of failure of the main booster regulator. Switchover is controlled by onboard detection of over or under voltage at the output of the main booster regulator.

Main inverter. The main inverter output is designed to provide 2.4-kHz ±0.01% single-phase squarewave power at 50 Vrms ±5% from a regulated 56-Vdc ±1% input. The *Mariner* Mars 1971 main inverter may be used without modification. In the event of a failure, the system will switch to a standby inverter with identical output characteristics.

400-Hz inverter. The *Mariner* Mars 1971 400-Hz inverter, including both single-phase and three-phase outputs, may be used without modification. The output characteristics of the single-phase portion are 28 Vrms ±5% squarewave and 400 Hz ±0.01%, including both amplitude and frequency, respectively. Average power output is 15 W at 28 V with a peak loading of 21 W. The 400-Hz three-phase power output characteristics are 400 Hz ±0.01% and 27.2 Vrms ±5% line-to-line, quasi-squarewave, including both frequency and amplitude, respectively. Average power of the three-phase output is 12 W with a peak of 15 W.

Dc–dc converter. The *Mariner* Mars 1971 dc–dc converter is utilized for the propulsion valves and gimbals. This unit converts the unregulated bus voltage to a regulated 30 Vdc. The power output required is 80 W.

f. Power distribution. The *Viking* orbiter power distribution philosophy is basically that of *Mariner* Mars 1971 modified for a battery charge/discharge control and the revised *Viking* orbiter power requirements. The solar panel output is distributed to the power source logic unit whereupon the unregulated dc power is distributed to the dc power distribution unit for *Viking* lander capsule usage. Unregulated or raw dc power is also distributed to the dc–dc converter as well as to the booster regulators, battery chargers, and the telecommunications system for separate conversion.

Power source logic. The power source logic unit contains the dc bus from which the solar panel and battery output are connected. The unit also contains the transfer switch for selection of internal or external power, the isolation diodes for the solar panel sections, and a portion of the power subsystem telemetry transducers.

Power control. The power control subassembly contains the failure sense circuit to detect out-of-tolerance conditions in the main power chain, the power control relay switch from the main power chain to the redundant or standby power chain, the attitude control relay that switches power to the attitude control system, and additional power subsystem transducers.

Heater–Viking lander capsule dc power distribution. This modified *Mariner* Mars 1971 unit contains the fuses for the power to the *Viking* orbiter heaters, a current telemetry transducer, and relays controlled by the flight command system for the battery test load. Unregulated power to the lander is distributed through a relay in this unit controlled by the central computer and sequencer (CC&S). Short-circuit protection and prevention of reverse current flow from the *Viking* lander capsule are also provided by this unit.

Power distribution subassembly. The power distribution subassembly receives signals from the flight command system and the CC&S for distribution of the *Viking* orbiter power. The signals are then processed in the module to actuate magnetic latching relays for power distribution. The input control signals are isolated switch closures between the command and the command line common to the two types: (1) pulse saturated transistor, and (2) pulse closure of relay contacts.

g. Subsystem weight. A preliminary weight breakdown of the *Viking* orbiter power subsystem, combined with the design status of each component, is shown in Table 6. The total weight of the power subsystem is approximately 60% greater than that of the *Mariner* Mars 1971. This is due primarily to the required increased solar panel area combined with the increase in battery capacity.

Table 6. Preliminary power subsystem weight

Unit	Weight, lb	Design status
Solar panel (4), 104 ft² (not including structure)	69.68	New design
Battery (2) including 15% case weight	138.00[a]	New design
Battery charge/discharge control (2)	9.00	New design
Booster regulator (2)	12.00	Modified
Heater–lander dc power distribution	2.00	Modified
Power source logic	8.00	Modified
Power distribution	1.83	Modified
Main inverter (2)	6.00	Mariner Mars 1971
Power control	2.35	Mariner Mars 1971
400-Hz inverter (single phase, three phase)	3.51	Mariner Mars 1971
Dc–dc converter	6.00	Mariner Mars 1971
	258.37	

[a]Assumes no sun occultation in sequence with the orbit-insertion mode.